AGU100 ADVANCING EARTH AND SPACE SCIENCE

JGR

Journal of Geophysical Research: Space Physics

RESEARCH ARTICLE

10.1002/2018JA025280

Key Points:

- We derive an empirical model of ionospheric convection including mid-latitude and polar SuperDARN HF radar velocity measurements for the first time
- Inclusion of mid-latitude radar data can increase the total measured cross-polar cap potential drop by as much as 40%
- Model provides a better specification of plasma flows in the deep polar cap and nightside Harang reversal region

Supporting Information:

- Supporting Information S1

Correspondence to:
E. G. Thomas,
evan.g.thomas@dartmouth.edu

Citation:
Thomas, E. G., & Shepherd, S. G. (2018). Statistical patterns of ionospheric convection derived from mid-latitude, high-latitude, and polar SuperDARN HF radar observations. *Journal of Geophysical Research: Space Physics*, *123*, 3196–3216. https://doi.org/10.1002/2018JA025280

Received 26 FEB 2018
Accepted 22 MAR 2018
Accepted article online 26 MAR 2018
Published online 26 APR 2018
Corrected 25 MAY 2018

This article was corrected on 25 MAY 2018. See the end of the full text for details.

Statistical Patterns of Ionospheric Convection Derived From Mid-latitude, High-Latitude, and Polar SuperDARN HF Radar Observations

E. G. Thomas[1] **and S. G. Shepherd**[1]

[1]Thayer School of Engineering, Dartmouth College, Hanover, NH, USA

Abstract Over the last decade, the Super Dual Auroral Radar Network (SuperDARN) has undergone a dramatic expansion in the Northern Hemisphere with the addition of more than a dozen radars offering improved coverage at mid-latitudes (50°–60° magnetic latitude) and in the polar cap (80°–90° magnetic latitude). In this study, we derive a statistical model of ionospheric convection (TS18) using line-of-sight velocity measurements from the complete network of mid-latitude, high-latitude, and polar radars for the years 2010–2016. These climatological patterns are organized by solar wind, interplanetary magnetic field (IMF), and dipole tilt angle conditions. We find that for weak solar wind driving conditions the TS18 model patterns are largely similar to the average patterns obtained using high-latitude radar data only. For stronger solar wind driving the inclusion of mid-latitude radar data at the equatorward extent of the ionospheric convection can increase the measured cross-polar cap potential (Φ_{PC}) by as much as 40%. We also derive an alternative model organized by the *Kp* index to better characterize the statistical convection under a range of magnetic activity conditions. These *Kp* patterns exhibit similar IMF B_y dependencies as the TS18 model results and demonstrate a linear increase in Φ_{PC} with increasing *Kp* for a given IMF orientation. Overall, the mid-latitude radars provide a better specification of the flows within the nightside Harang reversal region for moderate to strong solar wind driving or geomagnetic activity, while the polar radars improve the quality of velocity measurements in the deep polar cap under all conditions.

1. Introduction

Plasma circulation in the Earth's high-latitude ionosphere is largely controlled by interactions between open interplanetary magnetic field (IMF) lines embedded in the solar wind and closed geomagnetic field lines of the Earth's magnetosphere. Magnetic reconnection processes at the dayside magnetopause and in the nightside magnetotail generate electric fields, which are communicated from the magnetosphere to the ionosphere via field-aligned currents, driving plasma motion at *F* region altitudes. A two-cell convection pattern is often observed for southward IMF conditions (B_z-) with antisunward flow across the polar cap driven by dayside reconnection and sunward return flow at lower latitudes in the dawn and dusk auroral regions (Dungey, 1961). Asymmetries in this two-cell pattern occur when there is a strong east-west (B_y) component of the IMF as the dayside reconnection site is oppositely shifted toward dawn or dusk of the subsolar point in the two hemispheres. Under northward IMF conditions (B_z+), reconnection may occur poleward of the cusp between open field lines in the solar wind and the lobe cell of the Earth's magnetosphere, driving sunward flow across the polar cap in the form of reverse convection cells (Crooker, 1992; Crooker & Rich, 1993). Viscous interactions between the solar wind and magnetosphere also play a role in transferring energy to the coupled magnetosphere-ionosphere (M-I) system even in the absence of dayside reconnection (Axford & Hines, 1961; Papitashvili & Rich, 2002).

Because the dayside solar wind-magnetosphere coupling processes exhibit such close control over the strength and morphology of the high-latitude ionospheric potential, it is often useful to examine convection patterns in terms of solar wind parameters such as IMF magnitude and orientation. This approach is complicated by the varying time scales over which dayside and nightside reconnection processes occur (Grocott & Milan, 2014). By assuming the convection evolves from one steady state pattern to another following a transition in the solar wind driving, climatological or statistical patterns may be calculated from many instantaneous measurements for a given set of solar wind and/or geomagnetic conditions (e.g., Heppner & Maynard, 1987; Ruohoniemi & Greenwald, 1996; Weimer, 1995). These empirical models of ionospheric convection are useful not only as input to numerical models (e.g., Qian et al., 2014; Ridley et al., 2006) but also for space weather forecasting purposes due to the sometimes limited instantaneous measurements of the global electric field. A convenient scalar parameter often used for quantifying the global convection strength is the total cross-polar cap potential drop (Φ_{PC}). For two-cell convection, Φ_{PC} is easily calculated from the difference between the potential minima and maxima of the dusk and dawn cells.

Statistical convection models have been developed using a variety of observations and techniques, including measurements from low-altitude spacecraft (OGO 6, DE 2, and Defense Meteorological Satellite Program (DMSP)) (Hairston & Heelis, 1990; Heppner, 1977; Heppner & Maynard, 1987; Papitashvili et al., 1999; Papitashvili & Rich, 2002; Rich & Hairston, 1994; Weimer, 1995; 1996; 2001; 2005), high-altitude spacecraft (Cluster) (Förster et al., 2007, 2009; Förster & Haaland, 2015; Haaland et al., 2007), ground-based magnetometer arrays (Friis-Christensen et al., 1985; Papitashvili et al., 1994; Ridley et al., 2000), incoherent scatter radars (Foster, 1983; Foster et al., 1986; Holt et al., 1987; Oliver et al., 1983; Peymirat & Fontaine, 1997; Senior et al., 1990; Zhang et al., 2007), and coherent scatter radars (Cousins & Shepherd, 2010; Pettigrew et al., 2010; Ruohoniemi & Greenwald, 1996, 2005). Each of these models has its own limitations ranging from instrumental biases to the duration of the underlying data set. Here we focus our attention on the continually improving empirical convection results contributed by the high-frequency (HF) coherent scatter radars of the Super Dual Auroral Radar Network (SuperDARN; Chisham et al., 2007; Greenwald et al., 1995).

Ruohoniemi and Greenwald (1995) presented the first statistical characterization of ionospheric convection using line-of-sight (LOS) velocity measurements from a SuperDARN radar located in Goose Bay, Canada (GBR), as a function of IMF and season. This study was expanded by Ruohoniemi and Greenwald (1996) who derived a more complete set of statistical patterns (hereafter referred to as the RG96 model) organized by IMF magnitude and clock angle using data from the GBR radar. Ruohoniemi and Baker (1998) developed an assimilative procedure called “Map Potential” to solve for the instantaneous high-latitude potential pattern by combining LOS velocity measurements with a climatological model keyed to the prevailing solar wind conditions. Model vectors sampled from the RG96 patterns were used to help constrain the global Map Potential solution in regions where no radar observations are available; however, in principle, any convection model could be used for this purpose (Shepherd & Ruohoniemi, 2000).

Ruohoniemi and Greenwald (2005) advanced the state of the RG96 model by including velocity measurements from eight additional Northern Hemisphere radars monitoring the auroral zone poleward of 65° magnetic latitude (MLAT). They also considered seasonal and local time factors in the convection morphology, although their final model patterns (RG05) are parameterized by only IMF magnitude and clock angle. Pettigrew et al. (2010) tested the interhemispheric symmetry of climatological ionospheric convection by deriving independent model patterns (PSR10) for both the Northern and Southern Hemispheres following the procedure of Ruohoniemi and Greenwald (2005). In addition to IMF magnitude and clock angle, the PSR10 model results are further sorted by dipole tilt angle for a season-like parameter (dipole tilt also has a diurnal component due to the offset between Earth’s geographic and magnetic poles). Most recently, Cousins and Shepherd (2010) derived a new model (CS10) that expanded on the PSR10 results by considering an additional 3 years of data and modifying the sorting criteria to also include a solar wind velocity dependence.

While each of the above models (RG96, RG05, PSR10, and CS10) represents a significant advancement from the previous work, they share a major limitation in the availability of data below about 65° MLAT. The original array of SuperDARN radars was constructed near 60° MLAT and oriented poleward to measure plasma drifts in the auroral and polar ionosphere (Greenwald et al., 1995). However, it became clear that under geomagnetically disturbed conditions the high-latitude radars are unable to measure the full latitudinal extent of the auroral convection zone as it expands equatorward to lower MLATs (Ruohoniemi et al., 2001). Enhanced ionization in the *D* and *E* regions can also decrease data coverage due to absorption (Chisham et al., 2007). To address these problems, SuperDARN has undergone an expansion to mid-latitudes in the Northern Hemisphere beginning with the construction of the first mid-latitude radar located at Wallops Island, Virginia (WAL), in 2005. There are now 10 mid-latitude radars located between 36° and 50° MLAT in the Northern Hemisphere stretching from Japan to the eastern United States. A simultaneous expansion of the SuperDARN array to so-called higher latitudes (71°–77° MLAT) has occurred with the completion of four “PolarDARN” radars in the Northern Hemisphere beginning in 2006. These polar radars improve the global coverage of the network during all geomagnetic activity conditions, particularly during strongly northward IMF B_z+ when reverse convection cells are present.

Following the construction of WAL, Baker et al. (2007) were the first to examine the impact of mid-latitude SuperDARN radar observations on statistical patterns of ionospheric convection. Using only a few months of data, they were able to compare average patterns with and without velocity measurements from WAL under quiet ($Kp \leq 3$) and active ($Kp \geq 3$) geomagnetic conditions. For quiet conditions the WAL radar observed backscatter from ionospheric irregularities on the nightside between 50° and 60° MLAT. The low-velocity westward drift of these mid-latitude irregularities is attributed to the neutral dynamo electric field and had a minimal impact on both the overall convection morphology and the calculated Φ_{PC}. For the geomagnetically disturbed case ($Kp \geq 3$), however, Baker et al. (2007) found a 25% increase in the calculated Φ_{PC} by including the WAL measurements due to the expansion of the auroral electric fields to middle latitudes below the fields of view of the high-latitude radars. It should be noted that the authors were unable to parameterize their statistical patterns by any secondary criteria such as IMF clock angle due to the limited WAL data set available at the time.

While data from mid-latitude and polar radars are routinely included in instantaneous Map Potential solutions (e.g., Thomas et al., 2013), there have been no studies examining the impact of these data on statistical patterns of ionospheric convection since the preliminary findings reported by Baker et al. (2007). In this study we use data from the full array of mid-latitude, high-latitude, and polar SuperDARN radars in the Northern Hemisphere to derive a new empirical convection model, which is a better representation of the average convection, particularly under more strongly disturbed geomagnetic conditions. We maintain some similarities to the derivation of the CS10 model for easier comparison with this model while also deviating in other important aspects. The data sets and methodology used to derive the model convection patterns are described in section 2. In section 3 we present the discrete patterns of ionospheric convection organized by solar wind and geomagnetic parameters. In section 4 we discuss contributions of the new mid-latitude and polar radars before comparing our results to other convection models.

2. Data and Methodology

SuperDARN is an international network of HF radars operating continuously in both hemispheres to measure LOS velocity, backscattered power, and spectral width from decameter-scale irregularities in the *E* and *F* region ionosphere. Past SuperDARN convection models have focused on solar cycle maximum intervals due to the increased occurrence of HF radar backscatter (Ghezelbash et al., 2014; Koustov et al., 2004; Ruohoniemi & Greenwald, 1997). This solar cycle preference is illustrated in Figure 1 with monthly (red) and smoothed (blue) sunspot numbers overlaid on the time spans used to derive each of the SuperDARN statistical convection models (shaded gray). For our model we consider observations from the years 2010–2016 to coincide not only with the peak of solar cycle 24 but also the construction of new radar sites at both mid-latitudes and polar latitudes (Figure 2). We focus our analysis on the Northern Hemisphere as the radar coverage at mid-latitudes and polar latitudes in the Southern Hemisphere has not appreciably changed since the CS10 model. Detailed information regarding each Northern Hemisphere radar site is provided in Table 1.

LOS velocities, power, and spectral width for the years 2010–2016 are obtained from the raw data samples using the FITACF2.5 library contained in version 4.0 of the Radar Software Toolkit (RST; SuperDARN Data Analysis Working Group, 2017, 2018). The LOS radar data are mapped onto an equal-area MLAT/magnetic longitude (MLON) grid in Altitude-Adjusted Corrected Geomagnetic Coordinates (Baker & Wing, 1989) at 2-min cadence using the “gridding” technique introduced by Ruohoniemi and Baker (1998) with some modifications. These changes include numerous bug fixes as well as implementation of the World Geodetic System 84 reference ellipsoid and the refined Altitude-Adjusted Corrected Geomagnetic Coordinates methodology developed by Shepherd (2014) and have since been incorporated into version 4.1 of the RST (SuperDARN Data Analysis Working Group, 2017, 2018).

Rather than simply using all of the available gridded velocity vectors for our statistical analysis, we have applied several criteria to ensure that only the highest-quality velocity data are considered. Because each radar may spend up to 50% of any month operating in a nonstandard manner during “Special” or “Discretionary” Time according to the network schedule, we only consider data collected from a subset of the “Common Time” radar control programs, which use the standard 45-km range separation and complete

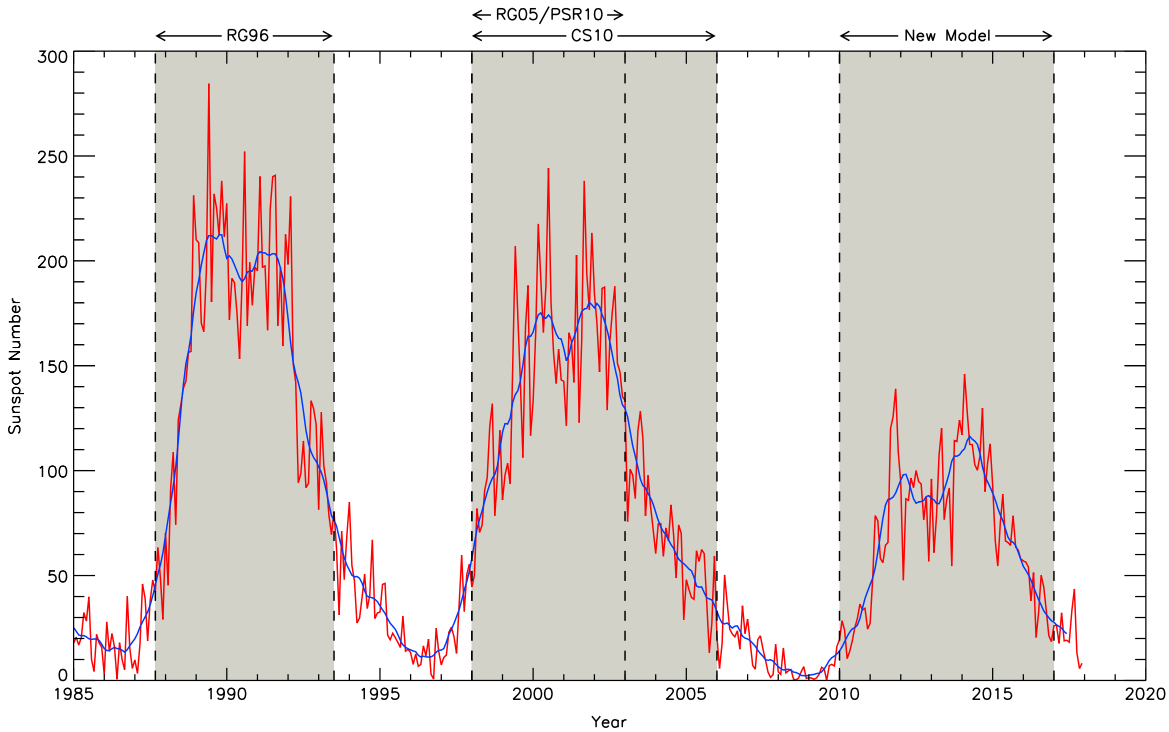

Figure 1. Monthly (red) and smoothed (blue) sunspot numbers since 1985. Time spans used in the past and current Super Dual Auroral Radar Network statistical convection studies are shaded gray and labeled at the top of the figure.

a full azimuthal scan every 1 or 2 min. For this study we also discard any data recorded from slant ranges nearer than 800 km to prevent contamination by lower-velocity *E* region echoes (Chisham & Pinnock, 2002). Similarly, we exclude any data from ranges greater than 2,000 km due to geolocation inaccuracies when using the standard empirical virtual height model (Chisham et al., 2008). The remaining observations therefore correspond to 1/2 hop backscatter from plasma irregularities in the *F* region ionosphere which drift at the $\mathbf{E} \times \mathbf{B}$ velocity and are mapped to the correct geographic location.

In this study the radar data are organized into discrete bins parameterized by the solar wind electric field magnitude ($E_{sw} = |V_x|\sqrt{B_y^2 + B_z^2}$), IMF clock angle ($\theta_{clk} = atan(B_y/B_z)$), and dipole tilt angle. One-minute resolution OMNI data are obtained from the OMNIWeb Plus interface (King & Papitashvili, 2005) to characterize the solar wind parameters, while dipole tilt angles are calculated from the 12th Generation International Geomagnetic Reference Field (IGRF-12) model (Thébault et al., 2015). Solar wind values are first lagged from the bow shock to the subsolar magnetopause using a similar approach as that used for the CS10 model, where the lag time is calculated as $\triangle t = \triangle x/(V_x/8)$. Here V_x is the antisunward component of the solar wind velocity and $\triangle x$ is the distance between the subsolar bow shock nose reported in the OMNI data and the empirical magnetopause model of Shue et al. (1997). The 10-min averages of E_{sw} and θ_{clk} are then calculated from the lagged 1-min OMNI values. The mean and median lag times are both around 7 min, which is smaller than the 10-min binning used in this study. Likewise, average dipole tilt values are calculated and assigned to each 10-min interval. Time intervals with no available OMNI data are excluded from further analysis.

For easier comparison with CS10 we choose similar model binning criteria with some necessary adjustments. The monthly sunspot numbers shown in Figure 1 indicate reduced levels of solar activity during the years considered for our new model (2010–2016) compared to the two previous solar cycles. Indeed, the distribution of 10-min average E_{sw} values from 2010 to 2016 is shifted toward significantly lower magnitudes as compared to the E_{sw} distribution for the CS10 model years (1998–2005; not shown). We therefore select the following E_{sw} bins for this study: 0–1.2, 1.2–1.6, 1.6–2.1, 2.1–3.0, and ≥3.0 mV/m. Note that the two largest CS10 magnitude bins (2.9–4.1 and ≥4.1 mV/m) have been effectively combined into a single bin (≥3.0 mV/m) for this study as a necessary consequence of the weaker solar cycle. We adopt the nonuniform IMF clock angle binning introduced for the CS10 model such that the bins centered at $B_z\pm$ and $B_y\pm$ are 50° and 40° wide, respectively; intermediate B_z/B_y bins are 45° wide. Finally, dipole tilt values are classified as negative (win-

10.1002/2018JA025280

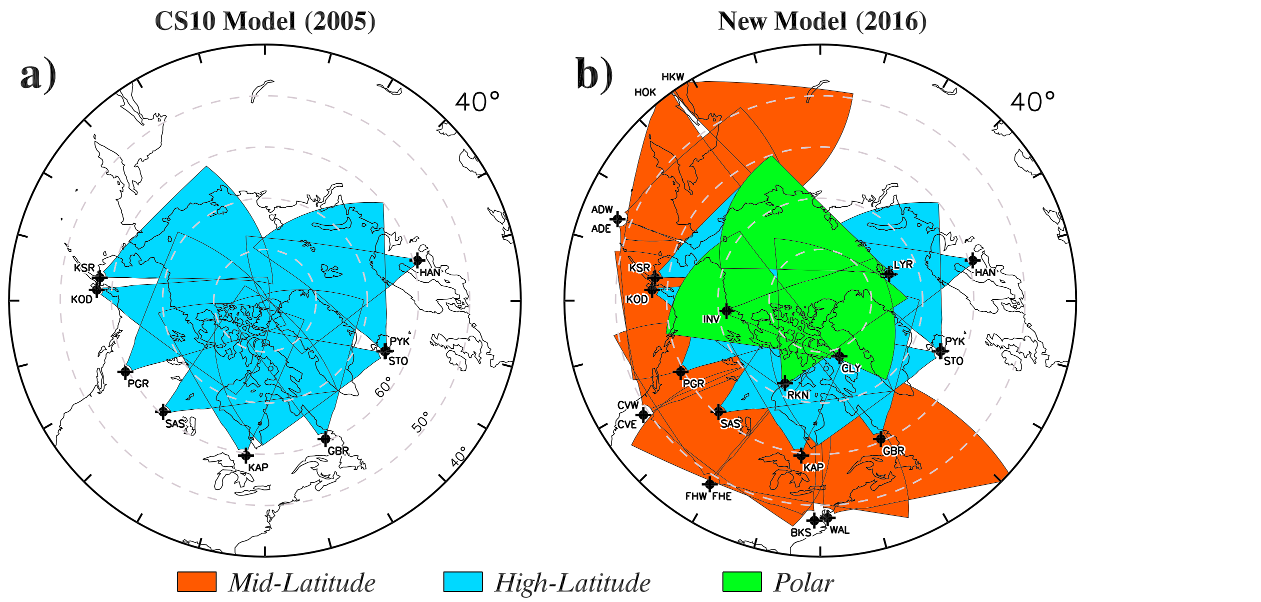

Figure 2. Fields of view of the Northern Hemisphere Super Dual Auroral Radar Network radars contributing to the (a) CS10 model and (b) new statistical model in geomagnetic coordinates. Dates in parentheses indicate the final year considered by each model. Mid-latitude, high-latitude, and polar radar fields of view are shaded orange, blue, and green, respectively. Detailed information regarding each radar site is provided in Table 1.

ter like; tilt $< -10°$), neutral (equinox like; $-10° \leq$ tilt $\leq 10°$), or positive (summer like; tilt $> 10°$) using the same criteria as used for the PSR10 and CS10 models.

Once all stable intervals are identified, the gridded LOS velocity measurements are translated to a MLAT/magnetic local time (MLT) coordinate system with a lower boundary of 45° MLAT. The weighted average velocity magnitude, azimuth, and error measured by each radar are then calculated for every equal-area MLAT/MLT grid cell during each 10-min interval. A final merged velocity vector is then locally solved within each MLAT/MLT cell by performing a least squares linear regression to all available 10-min average vectors for a given model bin. This procedure is similar to the original "merge" technique that combined instantaneous LOS velocity measurements from a pair of radars with overlapping beams (Cerisier & Senior, 1994). A threshold of at least 20 vectors and a minimum azimuth separation test (25°) must be passed in order to calculate a merged vector in a given grid cell. The error assigned to each grid cell is the arithmetic mean of the input velocity vector errors in that cell. Repeating this process for each E_{sw}, θ_{clk}, and tilt bin produces 120 statistical velocity patterns of up to 6,041 merged vectors and their errors. The total number of 10-min average velocity vectors per model pattern is overlaid on each panel of Figure 3 in red. As expected, the number of velocity vectors tracks the number of stable IMF intervals quite closely and is superimposed on a seasonal trend showing more radar measurements available during winter-like (Figure 3a) conditions than summer-like (Figure 3c) conditions. In order to more evenly distribute data values in the largest E_{sw} magnitude bin ($\geq$3.0 mV/m), we have therefore expanded the dipole tilt range by 5° to tilt $> 5°$ (Figure 3o). After making this adjustment the median number of 10-min average grid vectors contributing to each statistical pattern is about 340,000. A minimum of 96,000 vectors contribute to each model pattern with more than 200,000 vectors contributing to 114 of the 120 statistical patterns.

Before computing a best fit global solution of the electrostatic potential distribution to the merged vectors, it is necessary to specify a zero potential boundary at the lower-latitude limit of the convection zone (Ruohoniemi & Baker, 1998). Shepherd and Ruohoniemi (2000) introduced a Heppner-Maynard boundary (HMB), which is circular on the nightside but compressed on the dayside based on the results of Heppner and Maynard (1987) and is parameterized by the MLAT where it crosses the midnight MLT meridian. For an instantaneous Map Potential solution the HMB is set to the lowest possible latitude for which a minimum of three LOS vectors with velocities greater than 100 m/s lie along its boundary (Imber et al., 2013). Due to the more complete spatial coverage afforded by the statistical patterns in this study, we use the modified criteria of 25 merged vectors with velocities greater than 150 m/s to determine the HMB location. Following this automatic determination, we qualitatively adjust the boundary latitude to more accurately align with the low-latitude velocity dropoff. Any merged vectors lying below the HMB are discarded, and the dayside region between the compressed HMB and circular zero potential boundary is padded with zero-velocity vectors. Pettigrew et al.

Table 1
Details of SuperDARN Radars in the Northern Hemisphere (Figure 2b)

			Geographic		AACGM-v2	
Radar name	Code	Start	Latitude	Longitude	Latitude	Longitude
Polar						
Inuvik	inv	Jan 2008	68.41°	−133.77°	71.14°	−81.46°
Rankin Inlet	rkn	May 2006	62.83°	−92.11°	71.55°	−21.89°
Clyde River	cly	Aug 2012	70.49°	−68.50°	77.53°	18.37°
Longyearbyen	lyr	Oct 2016	78.15°	16.07°	75.47°	108.69°
High-latitude						
King Salmon	ksr	Oct 2001	58.68°	−156.65°	57.10°	−96.79°
Kodiak	kod	Jan 2000	57.60°	−152.20°	56.75°	−92.56°
Prince George	pgr	Mar 2000	53.98°	−122.59°	58.98°	−61.83°
Saskatoon	sas	Sep 1993	52.16°	−106.53°	60.05°	−41.39°
Kapuskasing	kap	Sep 1993	49.39°	−82.32°	58.73°	−6.40°
Goose Bay	gbr	Oct 1983	53.32°	−60.46°	59.48°	23.68°
Stokkseyri	sto	Aug 1994	63.86°	−21.03°	63.70°	65.73°
Pykkvibaer	pyk	Nov 1995	63.77°	−20.54°	63.54°	66.09°
Hankasalmi	han	Jun 1995	62.32°	26.61°	58.87°	103.86°
Mid-latitude						
Hokkaido West	hkw	Oct 2014	43.54°	143.61°	36.91°	−143.38°
Hokkaido East	hok	Nov 2006	43.53°	143.61°	36.90°	−143.38°
Adak West	adw	Sep 2012	51.89°	−176.63°	47.23°	−111.22°
Adak East	ade	Sep 2012	51.89°	−176.63°	47.23°	−111.22°
Christmas Valley West	cvw	Nov 2010	43.27°	−120.36°	48.75°	−56.40°
Christmas Valley East	cve	Nov 2010	43.27°	−120.36°	48.75°	−56.40°
Fort Hays West	fhw	Nov 2009	38.86°	−99.39°	47.92°	−30.24°
Fort Hays East	fhe	Nov 2009	38.86°	−99.39°	47.92°	−30.24°
Blackstone	bks	Feb 2008	37.10°	−77.95°	46.50°	−0.89°
Wallops Island	wal	Jun 2005	37.93°	−75.47°	46.97°	2.58°

Note. Latitude and longitude values are given in degrees north and east, respectively. Altitude-Adjusted Corrected Geomagnetic Coordinates version 2 (AACGM-v2) coordinates are calculated for the date 1 January 2016.

(2010) performed a sensitivity analysis of this dayside velocity padding and HMB determination, finding the associated variations in Φ_{PC} to be only about 5%.

Finally, the merged and zero-pad velocity vectors are fitted to an eighth order, eighth-degree expansion of Φ in terms of spherical harmonic functions using the technique of Ruohoniemi and Baker (1998). The electrostatic potential distribution across the MLAT/MLT grid is calculated from the fitted velocity vectors using the equations $\mathbf{V} = (\mathbf{E} \times \mathbf{B})/B^2$ and $\mathbf{E} = -\nabla\Phi$. Because the original LOS velocity vectors contributing to the solution at each MLAT/MLT cell are measured at different geographic locations spanning a 7-year interval,

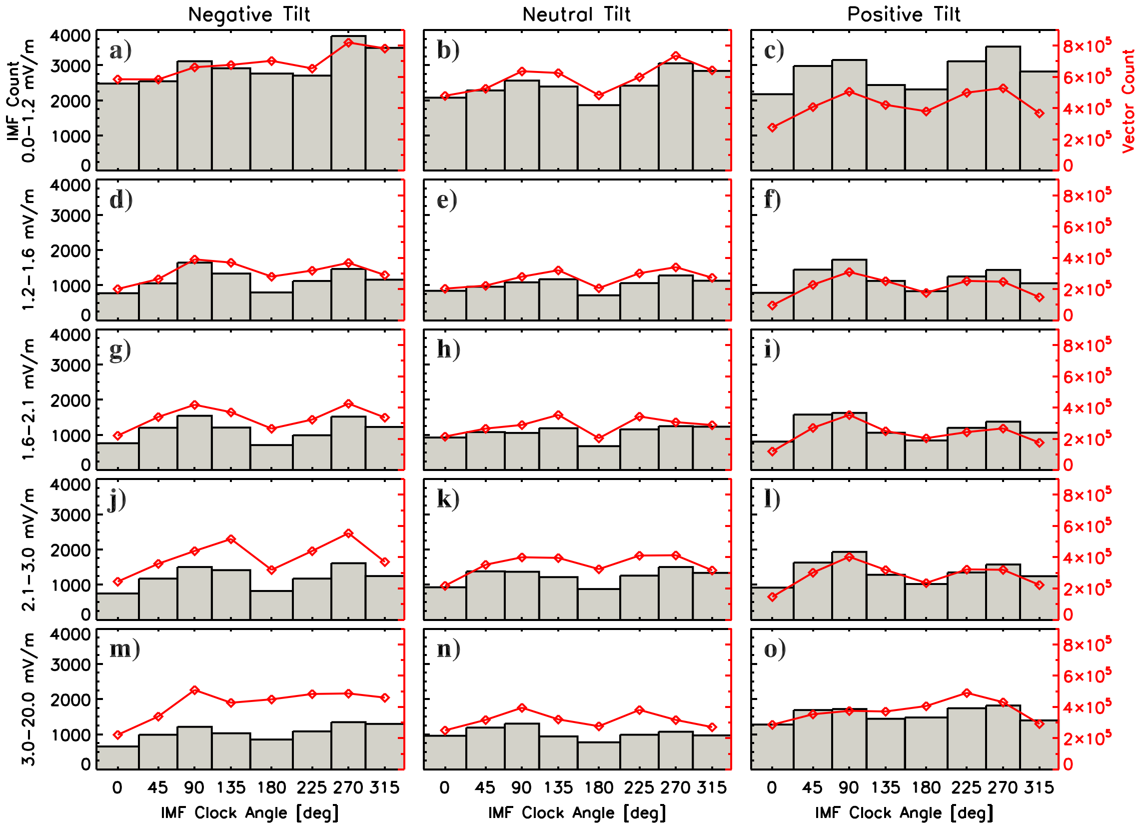

Figure 3. Distribution of stable 10-min intervals in each E_{sw} magnitude, interplanetary magnetic field (IMF) clock angle, and dipole tilt angle bin for the years 2010–2016. Total number of 10-min average velocity vectors (from cells where a merged vector was calculated) per model bin is overlaid on each panel in red.

it is difficult to assign exact values of **B** as the total field strength may change by as much as 630 nT (∼1%). Therefore, at each MLAT grid step we calculate the average **B** corresponding to the midpoint of our study (1 July 2013) across all MLONs using the IGRF-12 model and then assign that value to all MLT cells at that MLAT. We conclude by noting that, unlike the standard Map Potential procedure of Ruohoniemi and Baker (1998), no vectors from a prior statistical model have been included to help stabilize the fitting process as sufficient data coverage is already achieved for each model pattern.

An example of the entire procedure is shown in Figure 4 for the $1.6 \leq E_{sw} < 2.1$ mV/m, IMF B_z-, and neutral tilt model pattern. The number of 10-min average grid vectors located within each MLAT/MLT grid cell can be seen in Figure 4a and varies from 20 to 233 vectors. Three distinct latitudinal bands observed near 60°, 70°, and 80° MLAT correspond to the 1/2 hop *F* region scattering volumes of the mid-latitude, high-latitude, and polar radars. It is important to remember the complementary nature of these regions as we consider statistical convection patterns under a variety of solar wind and geomagnetic conditions. Gray shading indicates cells with fewer than 20 average grid vectors for this model pattern and are excluded from further processing. Figure 4b shows the velocity variability within each grid cell where at least 20 vectors are available. The observed variability is typically greatest within the auroral zone between 70° and 80° MLAT and maximizes near the dayside cusp. Figure 4c shows the merged velocity vectors solved locally within each MLAT/MLT grid cell with the derived HMB overlaid as a dashed red line. The merged vectors indicate the existence of a two-cell convection pattern with a pair of low-velocity convection reversal boundaries visible between the high-velocity antisunward flow across the polar cap and sunward return flow at lower latitudes in the dawn and dusk sectors. The fitted contours of electrostatic potential overlaid on the merged and padded vectors in Figure 4d confirm this morphology. The other model patterns are derived in an analogous way.

3. Results

3.1. TS18 Convection Model

Following the procedure described in section 2, we obtain 120 discrete patterns of ionospheric convection for the Northern Hemisphere corresponding to five E_{sw}, eight θ_{clk}, and three dipole tilt bins. The complete set

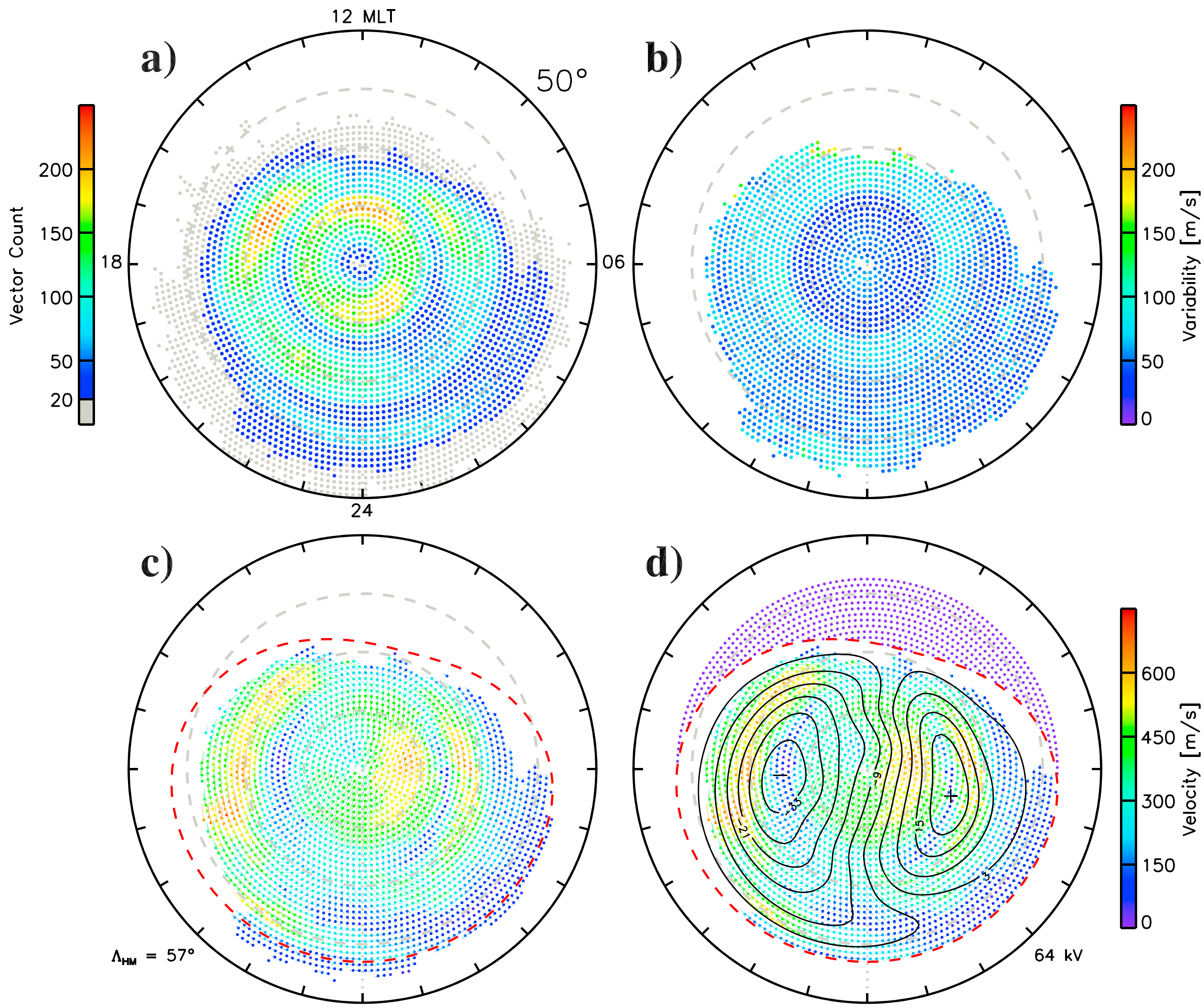

Figure 4. Distribution of (a) 10-min average velocity vectors, (b) velocity variability, (c) merged velocity vectors, and (d) merged and zero-padded velocity vectors with fitted contours of electrostatic potential overlaid for $1.6 \leq E_{sw} < 2.1$ mV/m, interplanetary magnetic field B_z-, and neutral dipole tilt conditions. Cells containing fewer than 20 vectors in Figure 4a are shaded gray and excluded from Figures 4b–4d. The nightside Heppner-Maynard boundary latitude and cross-polar cap potential (Φ_{PC}) are given to the lower left and lower right of panels (c) and (d), respectively.

of patterns are not shown here but are provided in the supporting information as Figures S1–S15. Here we continue the convention of referring to statistical models by an abbreviation of the authors' last names and year of publication; TS18, in this case.

Figure 5 shows a representative set of convection patterns arranged in clock dial format for neutral tilt and moderate solar wind driving conditions ($1.6 \leq E_{sw} < 2.1$ mV/m). It can be seen that both the size of the convection zone and magnitude of Φ_{PC} increase as θ_{clk} rotates from northward to southward IMF B_z orientations. As expected, the rounded/crescent shape of the dawn and dusk cells alternates according to the sign of the IMF B_y component (Reiff & Burch, 1985). Only the B_z+ pattern deviates significantly from the basic two-cell morphology, with signatures of twin reverse convection cells observed poleward of 78° MLAT on the dayside. These features are all well understood and have been described extensively in previous statistical models (e.g., Heppner & Maynard, 1987; Ruohoniemi & Greenwald, 1996). The TS18 patterns in Figure 5 show many similarities with past SuperDARN models but differ most significantly at lower latitudes on the nightside. In patterns for clock angles without a northward B_z component there is a low-latitude portion of the dusk convection cell which extends across the midnight MLT boundary located just poleward of 60° MLAT. Subauroral polarization stream (SAPS) electric fields are known to drive intense westward plasma flows in this region, forming the equatorward edge of the Harang reversal or discontinuity feature (Foster & Vo, 2002; Zou et al., 2009).

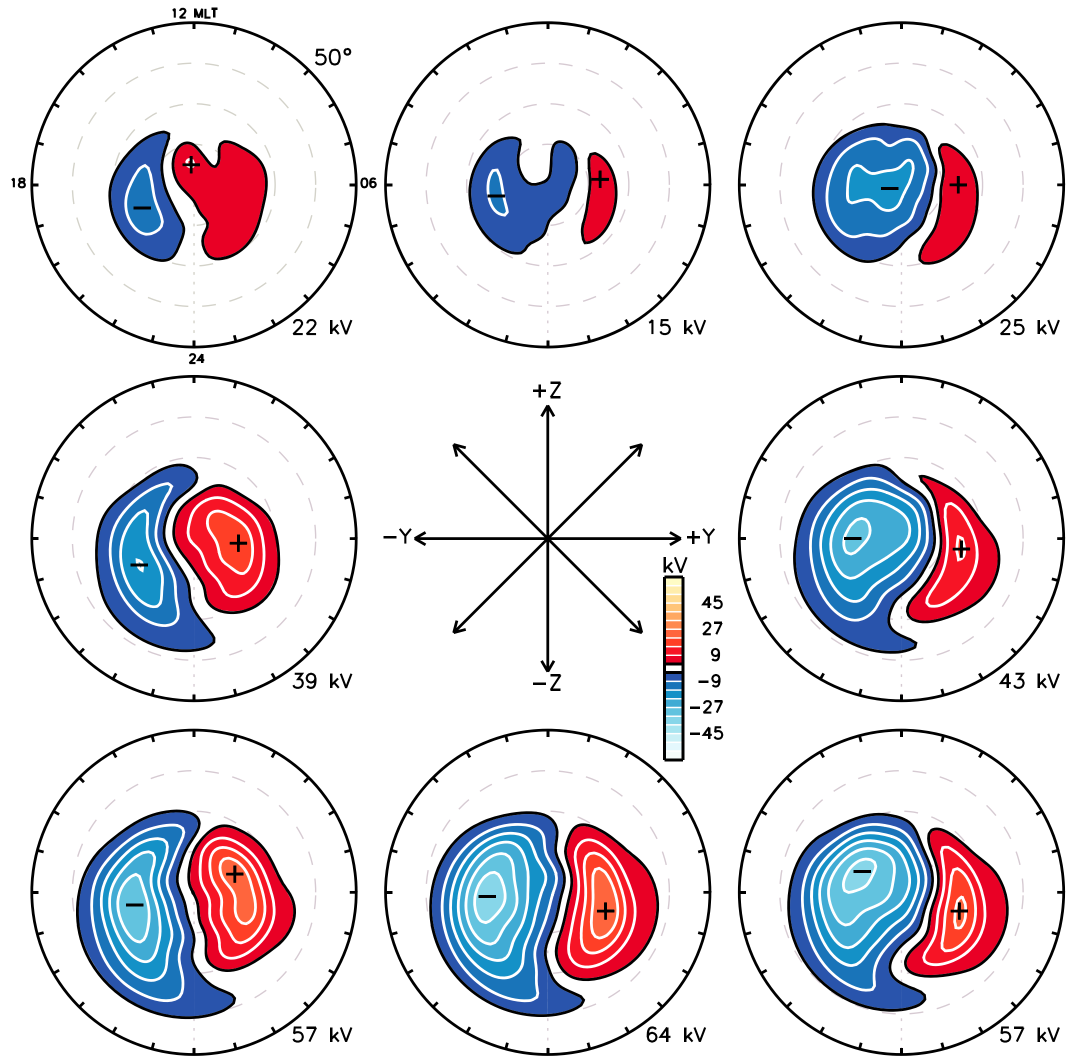

Figure 5. Statistical convection patterns sorted by interplanetary magnetic field clock angle for $1.6 \le E_{sw} < 2.1$ mV/m and neutral dipole tilt. Electrostatic potential is indicated by color according to the scale near the center of the figure, and equipotential contours are plotted at 6-kV intervals beginning at ±3 kV. The patterns are rotated so that noon (12 magnetic local time, MLT) is at the top with dawn (06 MLT) on the right and dusk (18 MLT) on the left. All plots have a low-latitude boundary of 50° magnetic latitude. The locations of the potential maxima (plus signs) and minima (minus signs) are marked, and the cross-polar cap potential difference is given at the bottom right of each panel.

The appearance of the Harang reversal in the TS18 model patterns is significant because SAPS was not definitively observed by a Northern Hemisphere SuperDARN radar until construction of the mid-latitude WAL radar (Oksavik et al., 2006). The patterns in Figure 5 are the first indication that inclusion of the mid-latitude radar data can alter the statistical convection morphology even for moderate solar wind driving conditions. One might expect greater differences between convection strength and extent to arise for more extreme driving conditions; we therefore consider the model results for the strongest E_{sw} magnitude bin ($E_{sw} \ge 3.0$ mV/m) and neutral tilt (shown in Figure 6). While the morphology of each pattern remains similar to their counterparts in Figure 5, the potential contours are seen to extend to lower latitudes for all θ_{clk} orientations (particularly on the nightside). When compared to the patterns in Figure 5, the increased number and density of the contours in both the dawn and dusk cells are reflected in the larger values of Φ_{PC}. Interestingly, the lower-latitude Harang reversal feature is less prominent for the B_z- patterns under the most extreme solar wind driving conditions in Figure 6 (neutral tilt). This result could be attributed to either an equatorward expansion of the SAPS flows below even the mid-latitude radars' FOVs or the duskward rotation of SAPS with increasing geomagnetic disturbance level that has been observed (e.g., Kunduri et al., 2017).

Generally, we observe similar dipole tilt dependencies as previously reported by Pettigrew et al. (2010) and Cousins and Shepherd (2010) (not shown). For low to moderate solar wind driving conditions ($E_{sw} < 2.1$ mV/m)

10.1002/2018JA025280

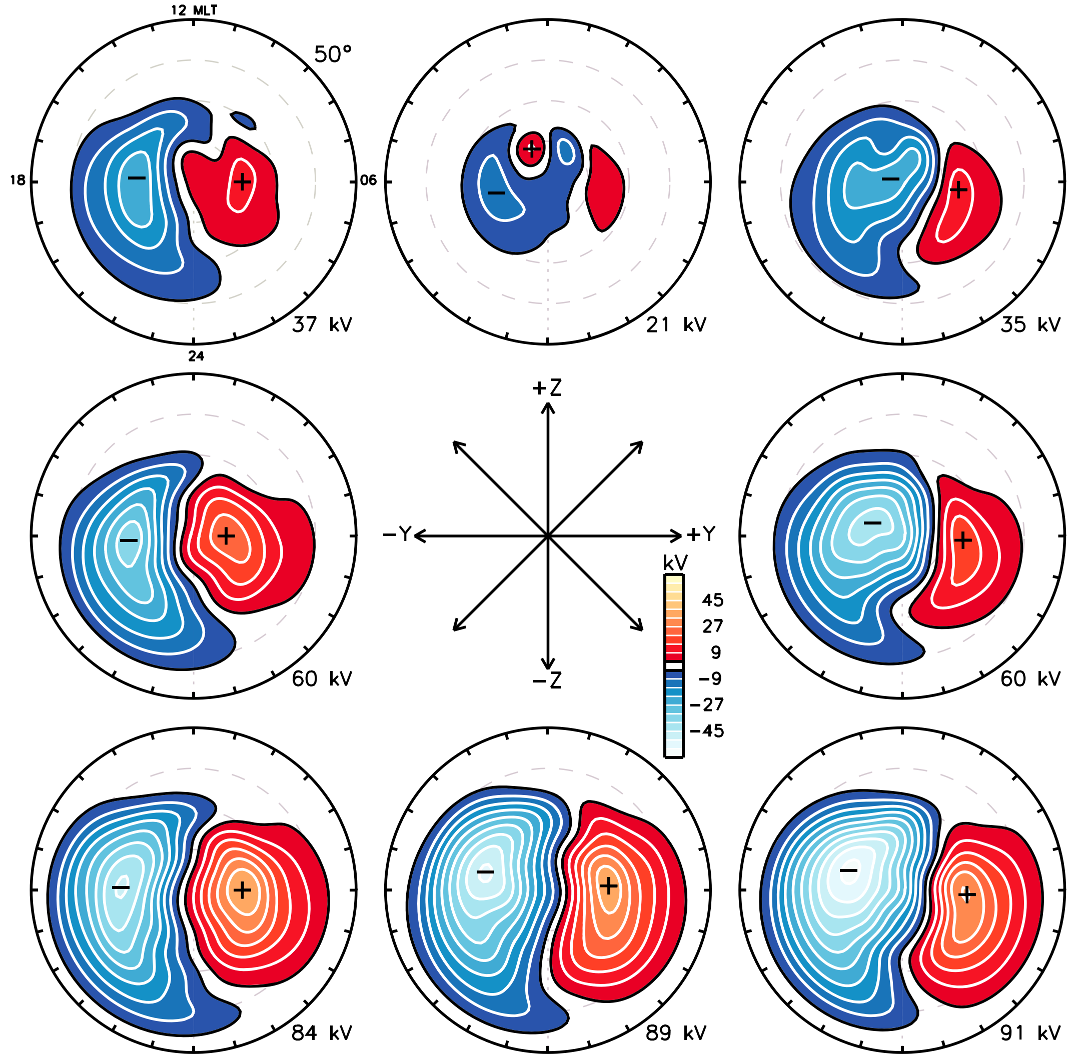

Figure 6. Statistical convection patterns for $3.0 \leq E_{sw} < 20.0$ mV/m and neutral tilt, in the same format as Figure 5. MLT = magnetic local time.

the dawn convection cell increases in strength and rotates toward earlier MLTs with increasing dipole tilt angle (particularly for IMF B_y-). Conversely, the dusk cell strengthens with decreasing dipole tilt angle (particularly for IMF B_y+). These B_y/tilt dependencies become less apparent for the larger E_{sw} magnitude bins (> 2.1 mV/m). Under northward IMF B_z conditions the reverse convection cells increase in strength as dipole tilt progresses from negative (winter-like) to positive (summer-like) angles. The sunward flows are aligned with the noon-midnight meridian for neutral and positive tilt angles, while for negative tilt they are oriented toward earlier MLTs.

Table 2 lists the Φ_{PC} values associated with each discrete convection pattern across all model E_{sw}, clock angle, and dipole tilt bins. Here we can see the trend of increasing Φ_{PC} from negative to positive dipole tilt for northward IMF B_z components. For southward IMF B_z orientations, the greatest Φ_{PC} values are associated with neutral dipole tilt conditions. The B_y dominant patterns also indicate larger Φ_{PC} values for neutral tilt, except for the largest E_{sw} magnitude bin where they are instead found for positive dipole tilt.

So far, we have presented our statistical model in terms of discrete patterns of ionospheric convection. One may also apply the trilinear interpolation technique described by Cousins and Shepherd (2010) to achieve more dynamical results. Using this technique, intermediate patterns and/or values of Φ_{PC} are obtained by linearly interpolating between model coefficients for adjacent E_{sw}, θ_{clk}, and dipole tilt bins. Map Potential can use this trilinear interpolation to avoid discontinuities as solar wind conditions vary from one model pattern to the next. Cousins and Shepherd (2010) were unable to derive B_z- patterns for their strongest E_{sw} bin ($\geq$ 4.1 mV/m) due to insufficient data coverage, limiting the ability to interpolate between CS10 model bins

Table 2
Φ_{PC} *Values Sorted by E_{sw}, IMF Clock Angle, and Dipole Tilt Conditions*

		E_{sw} magnitude bin				
IMF	Tilt	0.0–1.2	1.2–1.6	1.6–2.1	2.1–3.0	3.0–20.0
	Negative	16	15	17	16	20
B_z+	Neutral	20	16	15	18	21
	Positive	22	21	19	20	23
	Negative	19	19	20	28	36
B_z+/B_y+	Neutral	21	23	25	26	35
	Positive	22	24	25	29	35
	Negative	26	31	41	43	61
B_y+	Neutral	29	35	43	52	60
	Positive	27	35	40	44	65
	Negative	34	45	50	60	74
B_z-/B_y+	Neutral	38	49	57	67	91
	Positive	33	40	51	60	87
	Negative	38	51	60	67	79
B_z-	Neutral	42	57	64	78	89
	Positive	41	50	60	73	86
	Negative	33	44	49	55	65
B_z-/B_y-	Neutral	37	47	57	64	84
	Positive	36	47	51	62	83
	Negative	23	30	34	37	48
B_y-	Neutral	30	34	39	45	60
	Positive	29	36	41	48	61
	Negative	18	17	21	21	29
B_z+/B_y-	Neutral	20	21	22	26	37
	Positive	24	25	30	32	38

Note. All values are given in kV. IMF = interplanetary magnetic field.

for strongly southward IMF conditions. By contrast, a complete set of patterns is available with TS18 to perform trilinear interpolation between the full range of 120 model bins.

3.2. *Kp* Model

The TS18 model patterns indicate that significant plasma velocities are observed at or below 60° MLAT in a climatological sense for moderate to strong solar wind driving. These conditions do not necessarily correspond to the magnetic storm intervals when absorption at *D* and *E* region altitudes degrade the high-latitude radars' ability to monitor convection. It may then be useful to select different solar wind and/or geomagnetic sorting criteria for the derivation of alternative statistical model patterns. Several geomagnetic indices are available to characterize different aspects of the coupled MI-I system such as the *Ap*, *Kp*, *Dst*, *Sym-H*, *AE*, and *AL* indices. Historically, *Kp* has been the most commonly used magnetic activity index for examining convection due to its seemingly linear relationship with Φ_{PC} (e.g., Kivelson, 1976; Sojka et al., 1986; Thomsen, 2004). The *Kp* index is therefore ideal not only for sorting by magnetic activity but also allowing easier comparisons with other statistical models.

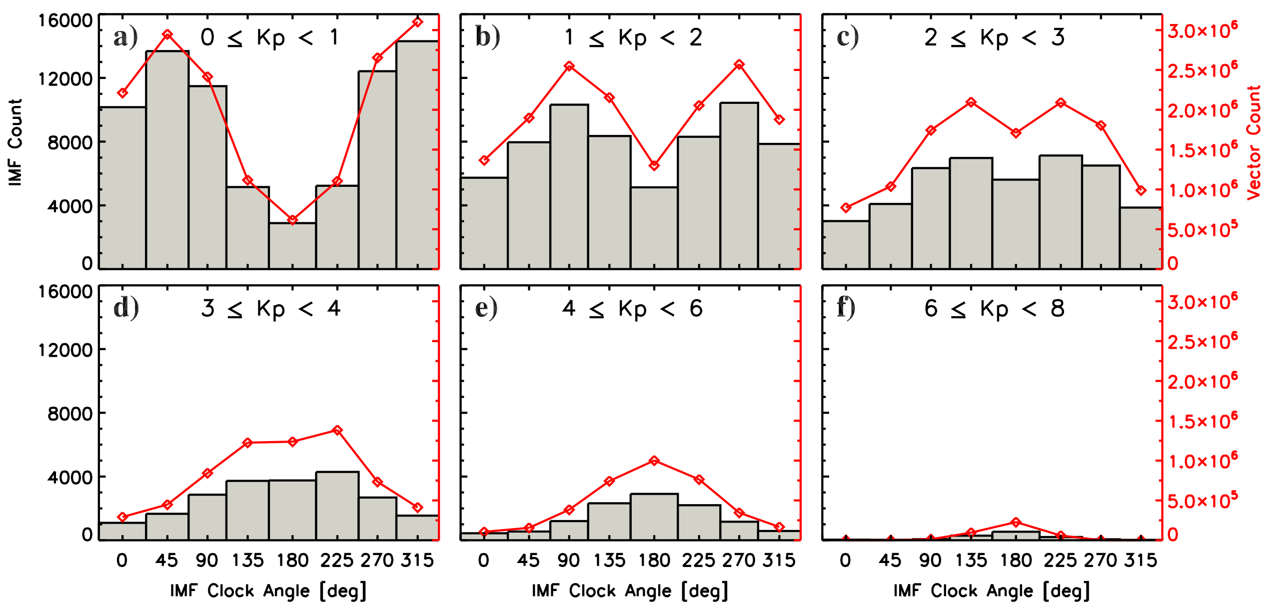

Figure 7. Distribution of stable 10-min intervals in each *Kp* and interplanetary magnetic field (IMF) clock angle bin for the years 2010–2016. Total number of 10-min average velocity vectors (from cells where a merged vector was calculated) per model bin is overlaid on each panel in red.

In the remainder of this section we present statistical patterns of ionospheric convection organized by the *Kp* geomagnetic activity index (rather than E_{sw}) and IMF clock angle θ_{clk}. The following *Kp* magnitude bins are selected: $0 \le Kp < 1$; $1 \le Kp < 2$; $2 \le Kp < 3$; $3 \le Kp < 4$; $4 \le Kp < 6$; and $6 \le Kp < 8$. Here the eight nonuniform θ_{clk} bins remain the same as for the TS18 and CS10 models. Figure 7 shows the distribution of stable time intervals and number of 10-min average velocity vectors per model bin in the same format as Figure 3. Again, a positive correlation is observed between the number of velocity vectors and stable *Kp*/IMF intervals. In contrast to the occurrence distributions shown in Figure 3, there is a clear relationship between *Kp* and θ_{clk} with the relative occurrence of IMF B_z- conditions growing more frequent as *Kp* increases. For this reason at the largest *Kp* magnitude range ($6 \le Kp < 8$) only the B_z- bin contains enough velocity vectors to constrain the fitted electrostatic potential solution. Note that we have not organized our *Kp* model results by dipole tilt angle due to insufficient statistics at the higher geomagnetic activity levels.

The full set of Kp/θ_{clk} convection patterns is again provided in the supporting information as Figures S16–S21. Figure 8 shows one set of patterns obtained for $2 \le Kp < 3$ conditions in the same clock dial format as Figures 5 and 6. These results may be compared most closely to Figure 6 of Ruohoniemi and Greenwald (1996) who considered the slightly wider activity range of $2- \le Kp \le 3+$ (and only this range). The convection patterns in Figure 8 appear remarkably similar to those for the moderate E_{sw} driving conditions in Figure 5 with some minor differences. Larger Φ_{PC} values are observed for the *Kp* model under northward B_z and B_y dominant θ_{clk} orientations, while the TS18 patterns exhibit stronger convection for southward IMF B_z. Also, *Kp* model patterns for northward IMF extend an additional 10° equatorward in MLAT on the nightside compared to the TS18 patterns. This discrepancy could be explained by the different time scales of the *Kp* (3-hr) and θ_{clk} (20-min) parameters used to organize the radar measurements. It could also be due to the mixing of dipole tilt effects in the *Kp* model patterns when compared to the TS18 results for neutral tilt only.

We next consider the variation in convection with increasing geomagnetic activity for selected θ_{clk} orientations. Figure 9 shows IMF B_y- (left), B_z- (center), and B_y+ patterns at four *Kp* activity levels: $0 \le Kp < 1$ (a–c), $2 \le Kp < 3$ (d–f), $4 \le Kp < 6$ (g–i), and $6 \le Kp < 8$ (j). There is a clear increase in the size and magnitude of the convection for all three IMF orientations, with the nightside Harang-type feature present for $Kp \ge 2$ conditions. The crescent/rounded shape of the dusk/dawn cells is maintained for the B_y dominant patterns regardless of activity level. For the $6 \le Kp < 8$ case (Figure 9j), the contours are observed to extend below 50° MLAT on the nightside. It is therefore likely that 97 kV is, in fact, an underestimate of the true Φ_{PC} due to the convection pattern expanding equatorward of even the mid-latitude radars' FOV during extreme geomagnetic activity.

To further examine the statistical relationship between convection strength and *Kp*, we show the Φ_{PC} values associated with each Kp/θ_{clk} pattern in Figure 10. The value of Φ_{PC} for undisturbed geomagnetic conditions ($0 \le Kp < 1$) ranges from 12 to 33 kV according to θ_{clk}. Similarly, the rate that Φ_{PC} increases between pat-

10.1002/2018JA025280

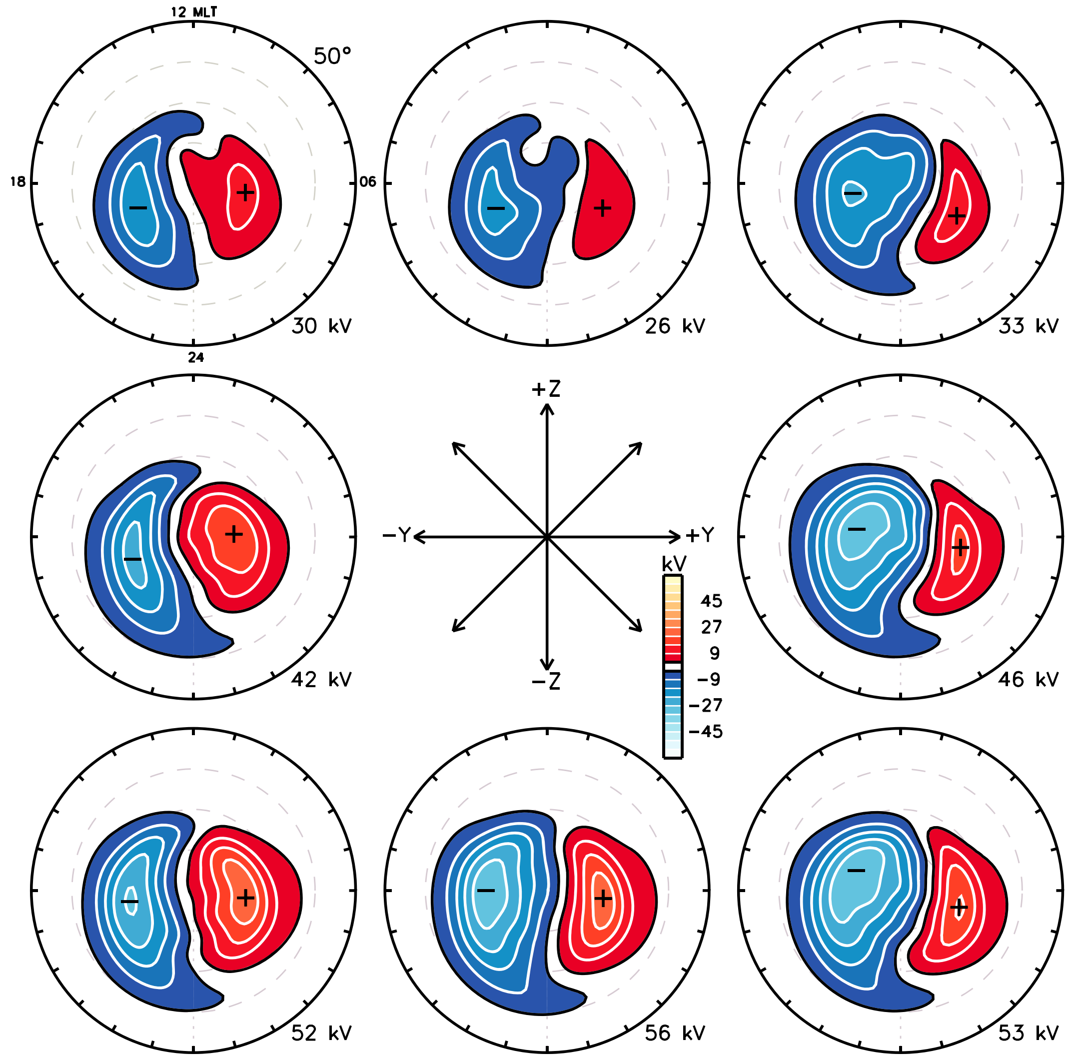

Figure 8. Statistical convection patterns for $2 \le Kp < 3$, in the same format as Figure 5. MLT = magnetic local time.

terns varies from 6 to 10 kV per *Kp* step for different IMF orientations (ignoring the $6 \le Kp < 8$ magnitude bin). These results suggest that Φ_{PC} varies linearly with *Kp* only when also taking into account the IMF clock angle θ_{clk}.

Unlike the TS18 model, which is designed to be compatible with the SuperDARN Map Potential software, we have not attempted to apply any linear interpolation techniques between discrete Kp/θ_{clk} model bins to obtain intermediate patterns due to the nonlinear nature of the *Kp* index (which is a quasi-logarithmic measure of geomagnetic activity). This decision may be evaluated at a later date if an operational need for more dynamical *Kp* model results is deemed necessary.

4. Discussion

The TS18 convection model and its *Kp* counterpart are the first statistical characterizations of ionospheric convection using SuperDARN data, which include velocity measurements from the mid-latitude and polar radars in the Northern Hemisphere (Figure 2). It is therefore desirable to assess the relative contributions of data from the mid-latitude and polar radars in terms of the model patterns shown in this paper. We first examine how the differing spatial coverage of the three latitudinal radar tiers can alter the global electrostatic potential solution before comparing our model results to other climatological descriptions of ionospheric convection.

Ruohoniemi and Greenwald (2005) constructed separate statistical patterns using individual radars located at high latitudes to examine Universal Time dependencies, while Baker et al. (2007) showed differing convection

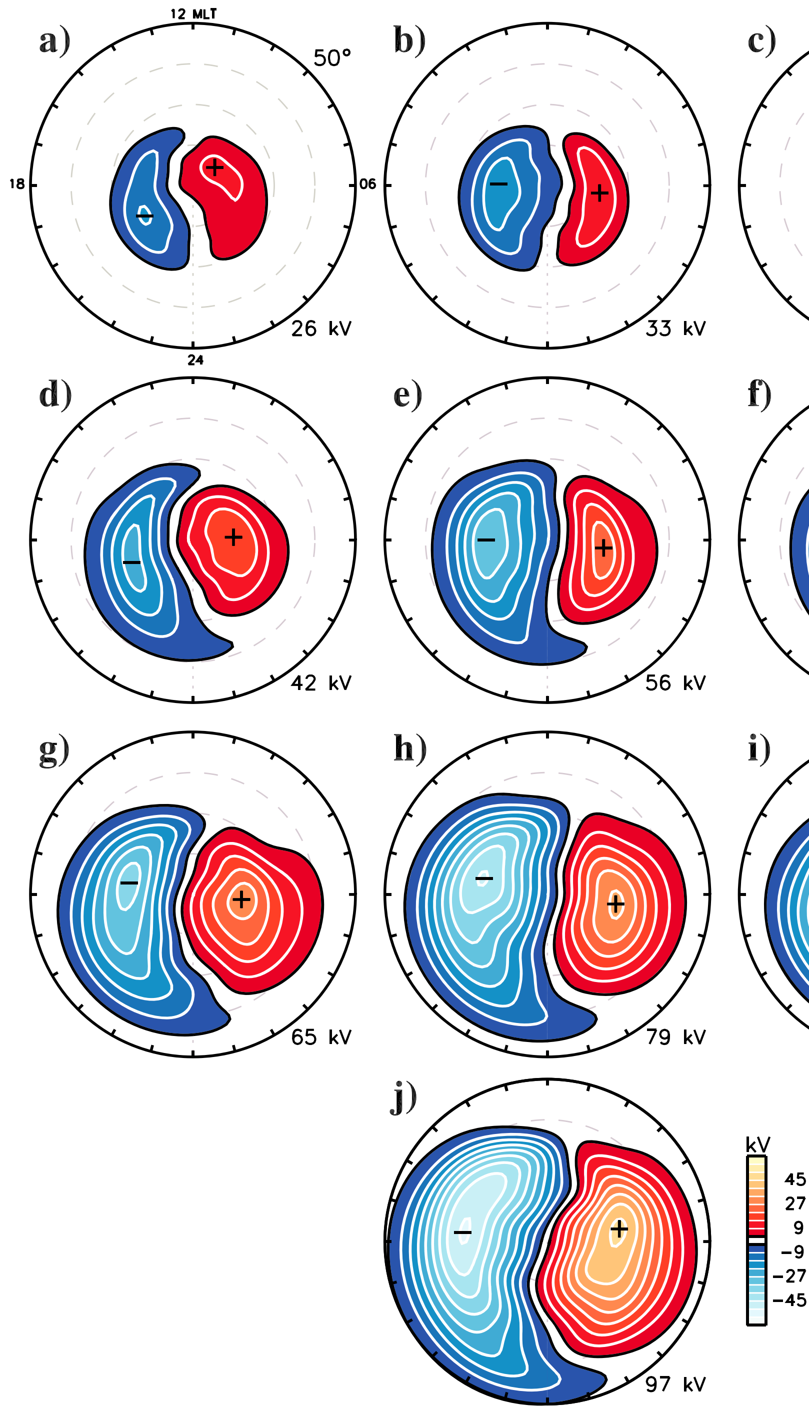

Figure 9. Statistical convection patterns sorted by interplanetary magnetic field (IMF) clock angle for selected increases in geomagnetic activity level: (a–c) $0 \leq Kp < 1$, (d–f) $2 \leq Kp < 3$, (g–i) $4 \leq Kp < 6$, and (j) $6 \leq Kp < 8$. Left, center, and right columns correspond to IMF B_y-, B_z-, and B_y+ orientations, respectively. Note that patterns could not be produced for the IMF $B_y\pm$ cases under $6 \leq Kp < 8$ conditions due to insufficient statistics. MLT = magnetic local time.

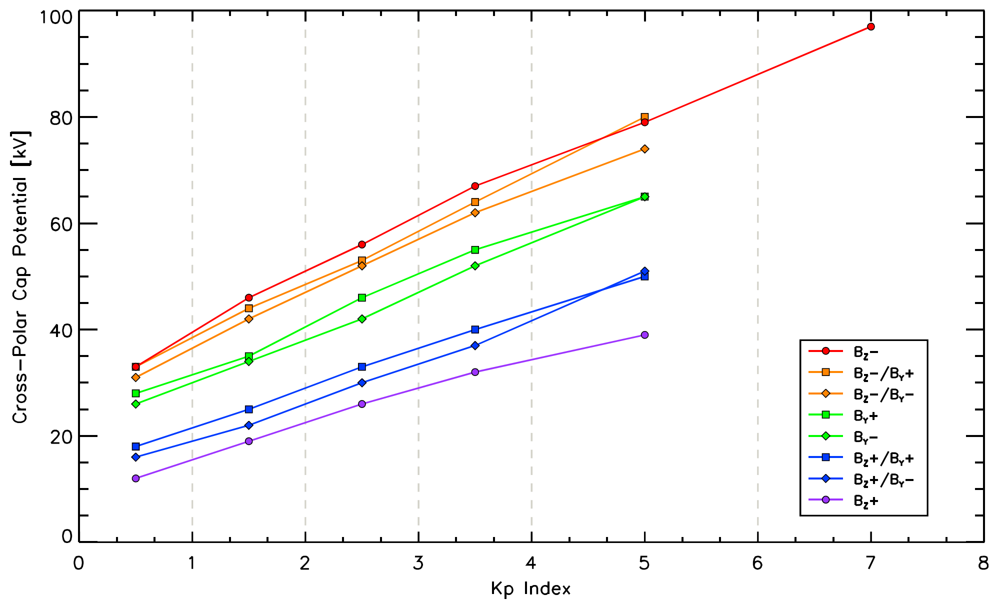

Figure 10. Cross-polar cap potential (Φ_{PC}) values sorted by *Kp* and interplanetary magnetic field clock angle; dashed gray lines indicate model *Kp* bin ranges.

results with and without the inclusion of data from the mid-latitude WAL radar for low ($Kp \leq 3$) and moderate ($Kp \geq 3$) magnetic activity. We adopt a similar approach by using data from subsets of radars (e.g., high latitude only, high latitude and polar, etc.) to calculate statistical patterns of merged velocity vectors using the methodology described in section 2 and compare the patterns to reveal the relative contributions of the additional radars. Contours of electrostatic potential are determined for cases where data coverage is sufficient to fully constrain the fitting procedure. The resulting patterns illustrate the contributions of data from the mid-latitudes and polar latitudes (i.e., measurements that were not available for previous models).

Figure 11 qualitatively demonstrates the complementary nature of the mid-latitude, high-latitude, and polar radar observations within the context of a full convection pattern under moderate solar wind driving conditions. The first three panels of Figure 11 show the merged velocity vectors calculated using data from the (a) high-latitude, (b) polar, and (c) mid-latitude radars for an example pattern, the same moderate solar wind driving conditions as the example in Figure 4. The last panel (Figure 11d) shows the merged vectors for this pattern using all of the available Northern Hemisphere radars. The TS18 model contours of electrostatic potential derived from the full set of vectors in Figure 11d are overlaid on each panel for reference.

Here we see that the high-latitude radar observations (Figure 11a) span a portion of the convection zone between 65° and 76° MLAT. While this level of coverage is sufficient to capture the dayside low-latitude extent and convection reversal boundaries, there is a kink in the antisunward flows near 85° MLAT near noon and on the nightside the dusk cell extends an additional 5° equatorward. These features indicate that the measurements used to derive the contours in these regions are not present in the high-latitude data. Measurements from the polar radars cover the region poleward of 77° MLAT and show a dawn-dusk asymmetry in the antisunward flows (Figure 11b). Likewise, the mid-latitude radar observations shown in Figure 11c reveal a Harang-like reversal between westward and eastward flows located below 65° MLAT on the nightside. The combined layers of mid-latitude, high-latitude, and polar radar data provide a more accurate and complete description of the average convection over the entire region poleward of 50° MLAT.

In addition to qualitative comparisons of data coverage as shown in Figure 11, it is possible to quantify the relative contribution of the three latitudinal radar tiers across each of the TS18 model bins in terms of Φ_{PC}. While this choice may not capture the full extent of the contributions of data from the mid-latitude and polar radars, it does provide a quantification of the overall convection strength. Because the polar radar data are necessary to constrain the electrostatic potential fit above about 80° MLAT (Figures 11a and 11b), we have relaxed the slant range criteria to include multihop *F* region backscatter when calculating the statistical patterns of merged velocity vectors for this portion of the analysis only. This modification allows multihop data from the mid-latitude and high-latitude radars to help constrain the solution at the expense of some uncertainty in the geolocation of LOS measurements from slant ranges >2,000 km (near-range echoes from ranges <800 km are still excluded).

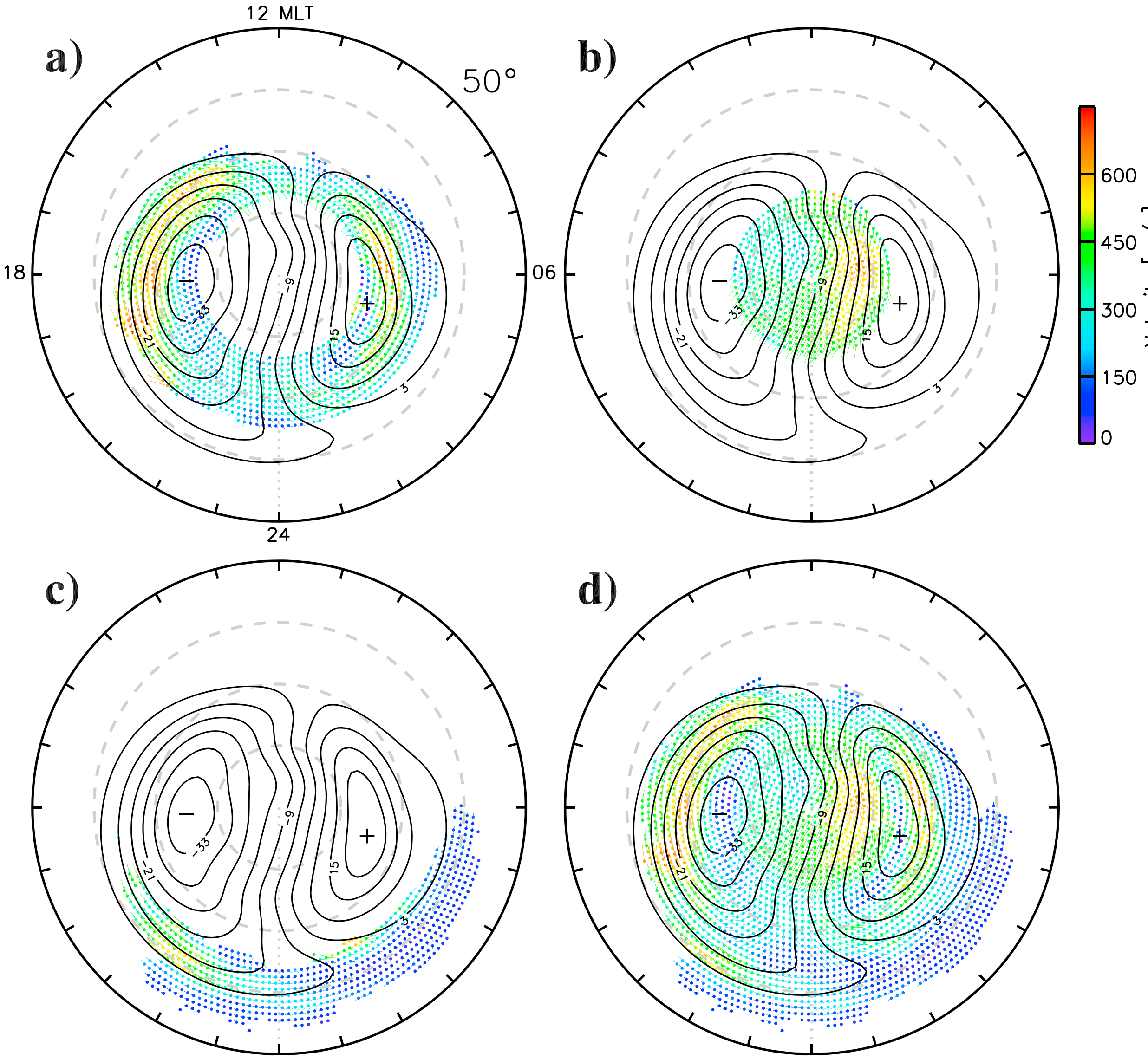

Figure 11. Merged 1/2 hop *F* region velocity vectors contributed by (a) high-latitude, (b) polar, (c) mid-latitude, and (d) all radars for $1.6 \leq E_{sw} < 2.1$ mV/m, interplanetary magnetic field B_z-, and neutral dipole tilt conditions. The final contours of electrostatic potential derived from the full set of radar observations in (d) are overlaid on each panel for reference. MLT = magnetic local time.

Figure 12 shows the Φ_{PC} values for the patterns derived using data from high-latitude (blue), high-latitude and polar (green), mid-latitude and high-latitude (red), and the complete set of radars (purple) in a polar format as a function of IMF clock angle. Each of the five panels corresponds to the increasing E_{sw} magnitude bins of the TS18 model. Note that in this format the radial and azimuthal components indicate Φ_{PC} and θ_{clk} rather than MLAT and MLT as in previous figures. By comparing the blue and green curves in Figure 12 one can identify the relative contribution of the polar radar data in terms of Φ_{PC}. Similarly, a comparison between the blue and red curves illustrates the contribution of the mid-latitude radar data.

Beginning with the weakest solar wind driving conditions in Figure 12a, the Φ_{PC} values at each θ_{clk} bin are nearly identical regardless of the input radar data. As E_{sw} increases (Figures 12b–12d) a separation between the curves begins to appear for southward IMF B_z orientations. Slightly larger values of Φ_{PC} (~5 kV) are obtained by adding the polar radar observations to the high-latitude measurements, while even greater increases (~10 kV) are found when combining the mid-latitude and high-latitude data. Under the strongest E_{sw} driving conditions (Figure 12e) the additional potential contributed by the polar radars is still ~5 kV while the mid-latitude radars contribute an additional 25–30 kV for southward IMF B_z orientations. To summa-

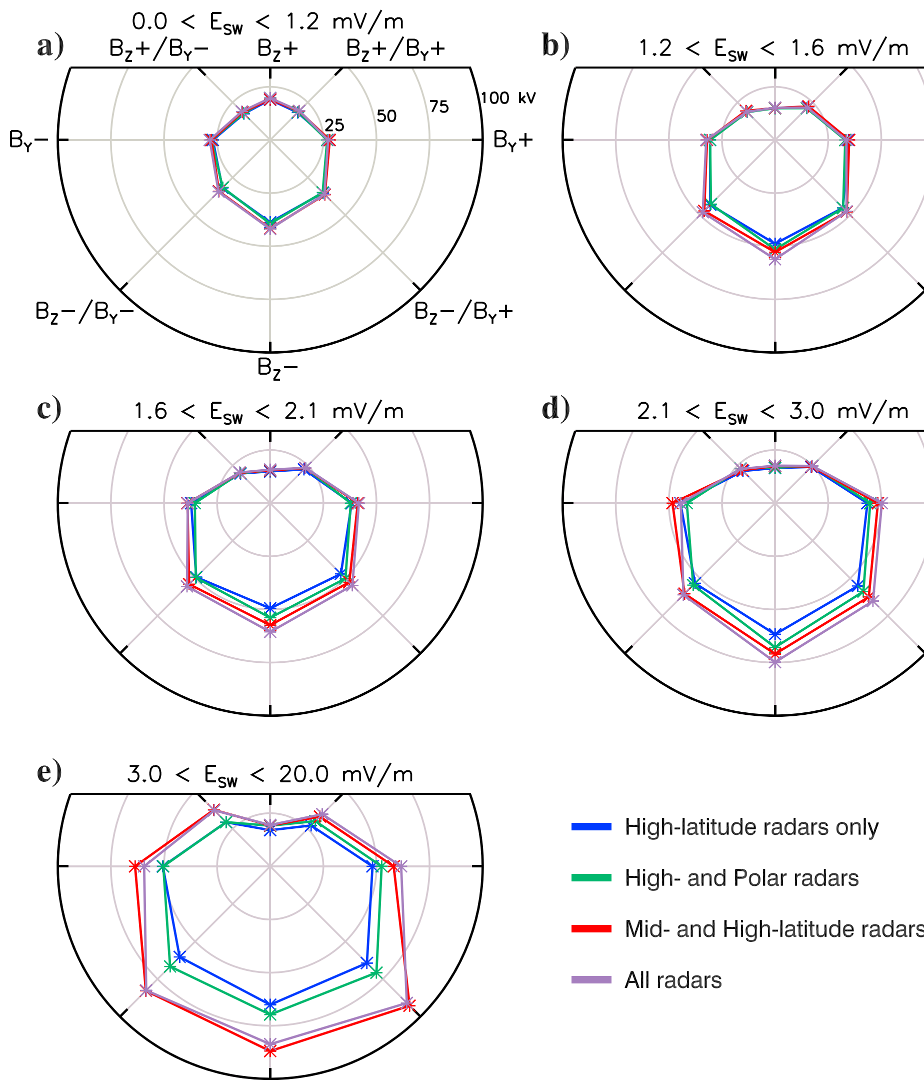

Figure 12. Cross-polar cap potential (Φ_{PC}) values for different radar combinations plotted against interplanetary magnetic field clock angle for increasing E_{sw} magnitude under neutral dipole tilt conditions. Note that multihop F region velocity vectors ($r > 2,000$ km) have been included for only this portion of the analysis to ensure the potential solution is fully constrained above 80° magnetic latitude.

rize, both mid-latitude and polar SuperDARN radars provide a valued contribution to the statistical patterns in terms of the global Φ_{PC} parameter, although the relative impact (measured by Φ_{PC}) of the mid-latitude observations increases much more rapidly with stronger solar wind driving.

Having discussed the mid-latitude and polar radars' influence on the global potential solution, we now compare the details of our statistical patterns to those described in previous studies. The most significant differences between the TS18 and past SuperDARN convection models are observed in the specification of the convection on the nightside. Ruohoniemi and Greenwald (1996, 2005) reported IMF B_y control of the nightside convection pattern in their statistical patterns, consistent with the dayside asymmetry of the dawn and dusk cells. This finding is in contrast to previous studies using low-altitude spacecraft (e.g., Heppner & Maynard, 1987) as well as conceptual frameworks of magnetotail processes (e.g., Lockwood et al., 1990). We find this B_y asymmetry to occur only for weak solar wind driving or geomagnetic activity levels (Figures 9a–9c) when the nightside convection pattern lies entirely poleward of 65° MLAT. However, under moderate to strong solar wind driving the Harang discontinuity is observed as an extension of the dusk cell across the midnight MLT meridian independent of IMF B_y (Figures 5 and 6). This feature is observed at progressively lower MLATs with increasing geomagnetic activity (Figure 9) in agreement with recent empirical studies of SAPS using

10.1002/2018JA025280

incoherent scatter (Erickson et al., 2011) and mid-latitude SuperDARN radar observations (Kunduri et al., 2017). Past statistical convection studies using SuperDARN measurements were unable to capture the Harang reversal due to the observational limitations of the high-latitude radars during periods of enhanced geomagnetic activity (e.g., Figure 11a).

This result is not to suggest that IMF B_y-related asymmetries do not occur in the nightside convection region but instead that we do not observe them in a climatological sense. Dynamic processes occurring in the magnetotail (e.g., substorms) and inner magnetosphere (e.g., SAPS) associated with time scales ranging from tens of minutes to several hours are likely obscured in our statistical patterns (Grocott, 2017). For example, Grocott and Milan (2014) demonstrated the continued evolution of ionospheric convection as a function of solar wind steadiness. In their study, they found the methodology of past statistical models to skew their results more closely to patterns corresponding to shorter time scales of solar wind steadiness. In the future, alternative parameters such as *Dst*, *AL*, or solar wind steadiness could be used to better capture these dynamical convection phenomena currently absent in most statistical patterns.

Although much of the discussion to this point has focused on the contribution of the mid-latitude radars to the TS18 model patterns, the polar radars also provide valuable measurements of the plasma flows above 80° MLAT (Figure 11). While their contribution to the total measured Φ_{PC} is relatively small (Figure 12), qualitatively the 1/2 hop measurements from the polar radars are a significant improvement over the sparse, imprecisely mapped multihop observations available from the high-latitude radars (Chisham et al., 2008). Inclusion of these data allows for better specification of the polar cap flows (particularly the reverse convection cells under northward IMF B_z) compared to previous statistical models. We find the magnitude of the reverse convection cells to strengthen with increasing dipole tilt in agreement with previous empirical studies (Crooker & Rich, 1993; Pettigrew et al., 2010). Recent studies by Koustov et al. (2017) and Yakymenko et al. (2018) using polar radar observations confirm this seasonal preference; however, they also report a deviation of the sunward flows toward prenoon MLTs in the summer hemisphere. Our results disagree, instead suggesting a prenoon orientation for negative dipole tilt (i.e., winter-like) conditions only. This discrepancy could be attributed to the limited number of events considered by Koustov et al. (2017, 3) and Yakymenko et al. (2018, 12) compared to the much larger number of northward IMF intervals in our strongest E_{sw} bins (Figures 3m–3o).

In addition to the TS18 model, we have derived a secondary model based on the *Kp* index for six magnitude bins ranging from $0 \leq Kp < 1$ to $6 \leq Kp < 8$. The *Kp* model patterns show a similar IMF B_y dependence as the TS18 model for all activity levels (Figure 9). As *Kp* increases, the potential contours expand to progressively lower latitudes and the IMF B_z+ patterns approach the standard two-cell configuration. This trend is likely due to the coarse temporal resolution of the *Kp* index (3 hr) compared to the averaged OMNI data (10 min). For the largest *Kp* conditions ($6 \leq Kp < 8$) the potential contours extend below 50° MLAT, which is outside the *F* region measurement area of all the mid-latitude radars except the Hokkaido East and West pair. The calculated Φ_{PC} value of 97 kV is therefore likely an underestimate of the true Φ_{PC}. Due to the approaching solar cycle minimum and infrequent occurrence of $Kp \geq 6$ events, it may be difficult to improve on the *Kp* model results for the larger activity levels, at least under the current relatively weak solar activity conditions.

SuperDARN measurements of ionospheric convection have been previously demonstrated to underestimate Φ_{PC} relative to other observational techniques (e.g., Drayton et al., 2005; Gao, 2012). Expanding on the preliminary results of Baker et al. (2007), we have demonstrated how the inclusion of mid-latitude and polar radar velocity observations can increase Φ_{PC} by as much as 40% for strong solar wind driving compared to using data from only the high-latitude radars. However, we have not accounted for the index of refraction effect discussed by Gillies et al. (2009), which may cause a 10–20% reduction of the LOS velocity magnitudes observed by SuperDARN. Correcting for this effect requires either (1) an accurate specification of the electron density within the HF radar backscattering volume or (2) angle-of-arrival information for the backscattered radar signal using a secondary interferometer antenna array. Even with current empirical models it is impossible to know the true electron density profile at all of the velocity measurement locations used in our study. Likewise, it is also very difficult to accurately calibrate and measure the elevation angle of HF radar returns, although this is currently a renewed focus of the SuperDARN community (Greenwald et al., 2017; Ponomarenko et al., 2016; Shepherd, 2017). Future use of accurate elevation angle data to correct LOS velocities for the index of refraction will have the added benefit of improved geolocation of ionospheric backscatter.

5. Summary

In this study we have developed a statistical model of ionospheric convection using SuperDARN radar observations parameterized by the solar wind electric field (E_{sw}), IMF clock angle (θ_{clk}), and dipole tilt angle. This model (TS18) differs from previous SuperDARN models in the following important aspects:

1. LOS velocity measurements are used from all available Northern Hemisphere radars spanning from mid-latitudes to the auroral zone to the polar cap.
2. Careful data selection has been performed to ensure only 1/2 hop *F* region observations from standard radar operating modes are included in the statistical analysis.
3. The processing software used to calculate gridded velocity vectors from LOS measurements has undergone substantial upgrades to improve the quality of data included in this study.

Using 7 years of data from 2010 to 2016, we have demonstrated that for weak solar wind driving conditions (E_{sw} < 1.6 mV/m) the TS18 model patterns do not significantly deviate from previous results because the low-latitude convection boundary lies within the field of view of the high-latitude radars. For stronger solar wind driving ($E_{sw} \geq$ 1.6 mV/m) the high-latitude radars are unable to fully image the auroral convection zone, thus underestimating the total cross-polar cap potential (Φ_{PC}) by as much as 40%. In addition, the mid-latitude radar observations indicate the presence of a low-latitude extension of the dusk convection cell in the nightside ionosphere under not only southward IMF but also B_y dominant orientations. Under northward IMF conditions, the polar radar data provide improved resolution of the reverse convection cells at high latitudes in the dayside ionosphere. An alternative model binned by the *Kp* index and θ_{clk} was also presented. The *Kp* model patterns exhibit similar IMF B_y asymmetries to the TS18 model; however, for increasing magnetic activity levels ($Kp \geq 3$) the B_z+ patterns adopt the classical two-cell morphology often associated with southward IMF B_z. Both the TS18 and *Kp* convection models represent a significant advancement over previous SuperDARN models of global-scale ionospheric convection and better description of the statistical convection under a wide range of solar wind driving and geomagnetic conditions. The TS18 model coefficients have been incorporated into the freely available SuperDARN RST for use with the standard analysis routines.

Acknowledgments
E. G. T. thanks the National Science Foundation for support under grant AGS-1524667. S. G. S. thanks the National Science Foundation for support under grant AGS-1341925. The sunspot data were obtained from the World Data Center SILSO, Royal Observatory of Belgium, Brussels at http://www.sidc.be/silso. The OMNI data were obtained from the NASA GSFC/SPDF OMNIWeb Plus interface at http://omniweb.gsfc.nasa.gov. The authors acknowledge the use of SuperDARN data. SuperDARN is a collection of radars funded by national scientific funding agencies of Australia, Canada, China, France, Italy, Japan, Norway, South Africa, United Kingdom, and the United States of America.

References

Axford, W. I., & Hines, C. O. (1961). A unifying theory of high-latitude geophysical phenomena. *Canadian Journal of Physics*, *39*, 1433–1464.

Baker, J. B. H., Greenwald, R. A., Ruohoniemi, J. M., Oksavik, K., Gjerloev, J. W., Paxton, L. J., & Hairston, M. R. (2007). Observations of ionospheric convection from the Wallops SuperDARN radar at middle latitudes. *Journal of Geophysical Research*, *112*, A01303. https://doi.org/10.1029/2006JA011982

Baker, K. B., & Wing, S. (1989). A new magnetic coordinate system for conjugate studies at high latitudes. *Journal of Geophysical Research*, *94*(A7), 9139–9143. https://doi.org/10.1029/JA094iA07p09139

Cerisier, J.-C., & Senior, C. (1994). Merge: A FORTRAN program (40 pp.). Cent. d'Etude des Environ. Terr. et Planet., Cent. Nat. de la Rech Si., St-Maur, France.

Chisham, G., & Pinnock, M. (2002). Assessing the contamination of SuperDARN global convection maps by non-F-region backscatter. *Annales de Geophysique*, *20*, 13–28. https://doi.org/10.5194/angeo-20-13-2002

Chisham, G., Lester, M., Milan, S. E., Freeman, M. P., Bristow, W. A., Grocott, A., et al. (2007). A decade of the Super Dual Auroral Radar Network (SuperDARN): Scientific achievements, new techniques and future directions. *Surveys in Geophysics*, *28*(1), 33–109. https://doi.org/10.1007/s10712-007-9017-8

Chisham, G., Yeoman, T. K., & Sofko, G. J. (2008). Mapping ionospheric backscatter measured by the SuperDARN HF radars—Part 1: A new empirical virtual height model. *Annales de Geophysique*, *26*, 823–841. https://doi.org/10.5194/angeo-26-823-2008

Cousins, E. D. P., & Shepherd, S. G. (2010). A dynamical model of high-latitude convection derived from SuperDARN plasma drift measurements. *Journal of Geophysical Research*, *115*, A12329. https://doi.org/10.1029/2010JA016017

Crooker, N. U. (1992). Reverse convection. *Journal of Geophysical Research*, *97*(A12), 19,363–19,372. https://doi.org/10.1029/92JA01532

Crooker, N. U., & Rich, F. J. (1993). Lobe cell convection as a summer phenomenon. *Journal of Geophysical Research*, *98*(A8), 13,403–13,407. https://doi.org/10.1029/93JA01037

Drayton, R. A., Koustov, A. V., Hairston, M. R., & Villain, J.-P. (2005). Comparison of DMSP cross-track ion drifts and SuperDARN line-of-sight velocities. *Annales de Geophysique*, *23*, 2479–2486. https://doi.org/10.5194/angeo-23-2479-2005

Dungey, J. W. (1961). Interplanetary magnetic fields and the auroral zones. *Physical Review Letters*, *6*, 47–48.

Erickson, P. J., Beroz, F., & Miskin, M. Z. (2011). Statistical characterization of the American sector subauroral polarization stream using incoherent scatter radar. *Journal of Geophysical Research*, *116*, A00J21. https://doi.org/10.1029/2010JA015738

Förster, M., & Haaland, S. E. (2015). Interhemispheric differences in ionospheric convection: Cluster EDI observations revisited. *Journal of Geophysical Research: Space Physics*, *120*, 5805–5823. https://doi.org/10.1002/2014JA020774

Förster, M., Paschmann, G., Haaland, S. E., Quinn, J. M., Torbert, R. B., Vaith, H., & Kletzing, C. A. (2007). High-latitude plasma convection from Cluster EDI measurements: Variances and solar wind correlations. *Annales de Geophysique*, *25*, 1691–1707. https://doi.org/10.5194/angeo-25-1691-2007

Förster, Y., Feldstein, I., Haaland, S. E., Dremukhina, L. A., Gromova, L. I., & Levitin, A. E. (2009). Magnetospheric convection from Cluster EDI measurements compared with the ground-based ionospheric convection model IZMEM. *Annales de Geophysique*, *27*, 3077–3087. https://doi.org/10.5194/angeo-27-3077-3087

Foster, J. C. (1983). An empirical electric field model derived from Chatanika radar data. *Journal of Geophysical Research*, *88*(A2), 981–987. https://doi.org/10.1029/JA088iA02p00981

Foster, J. C., & Vo, H. B. (2002). Average characteristics and activity dependence of the subauroral polarization stream. *Journal of Geophysical Research*, *107*(A12), 1475. https://doi.org/10.1029/2002JA009409
Foster, J. C., Holt, J. M., Musgrove, R. G., & Evans, D. S. (1986). Ionospheric convection associated with discrete levels of particle precipitation. *Geophysical Research Letters*, *13*(7), 656–659. https://doi.org/10.1029/GL013i007p00656
Friis-Christensen, E., Kamide, Y., Richmond, A. D., & Matsushita, S. (1985). Interplanetary magnetic field control of high-latitude electric fields and currents determined from Greenland Magnetometer Data. *Journal of Geophysical Research*, *90*(A2), 1325–1338. https://doi.org/10.1029/JA090iA02p01325
Gao, Y. (2012). Comparing the cross polar cap potentials measured by SuperDARN and AMIE during saturation intervals. *Journal of Geophysical Research*, *117*, A08325. https://doi.org/10.1029/2012JA017690
Ghezelbash, M., Fiori, R. A. D., & Koustov, A. V. (2014). Variations in the occurrence of SuperDARN F region echoes. *Annales Geophysicae*, *32*, 147–156. https://doi.org/10.5194/angeo-32-147-2014
Gillies, R. G., Hussey, G. C., Sofko, G. J., McWilliams, K. A., Fiori, R. A. D., Ponomarenko, P., & St.-Maurice, J.-P. (2009). Improvement of SuperDARN velocity measurements by estimating the index of refraction in the scattering region using interferometry. *Journal of Geophysical Research*, *114*, A07305. https://doi.org/10.1029/2008JA013967
Greenwald, R. A., Baker, K. B., Dudeney, J. R., Pinnock, M., Jones, T. B., Thomas, E. C., et al. (1995). DARN/SuperDARN: A global view of the dynamics of high-latitude convection. *Space Science Reviews*, *71*(1), 761–796. https://doi.org/10.1007/BF00751350
Greenwald, R. A., Frissell, N., & de Larquier, S. (2017). The importance of elevation angle measurements in HF radar investigations of the ionosphere. *Radio Science*, *52*, 305–320. https://doi.org/10.1002/2016RS006186
Grocott, A. (2017). Time-dependence of dawn-dusk asymmetries in the terrestrial ionospheric convection pattern. In S. Haaland (Ed.), *Dawn-Dusk Asymmetries in Planetary Plasma Environments*. Hoboken, NJ: John Wiley. https://doi.org/10.1002/9781119216346.ch9
Grocott, A., & Milan, S. E. (2014). The influence of IMF clock angle timescales on the morphology of ionospheric convection. *Journal of Geophysical Research: Space Physics*, *119*, 5861–5876. https://doi.org/10.1002/2014JA020136
Hairston, M. R., & Heelis, R. A. (1990). Model of the high-latitude ionospheric convection pattern during southward interplanetary magnetic field using DE 2 data. *Journal of Geophysical Research*, *95*(A3), 2333–2343. https://doi.org/10.1029/JA095iA03p02333
Heppner, J. P. (1977). Empirical models of high-latitude electric field. *Journal of Geophysical Research*, *82*(7), 1115–1125. https://doi.org/10.1029/JA082i007p01115
Haaland, S. E., Paschmann, G., Förster, M., Quinn, J. M., Torbert, R. B., McIlwain, C. E., et al. (2007). High-latitude plasma convection from Cluster EDI measurements: Method and IMF-dependence. *Annales de Geophysique*, *25*, 239–253. https://doi.org/10.5194/angeo-25-239-2007
Heppner, J. P., & Maynard, N. C. (1987). Empirical high-latitude electric field models. *Journal of Geophysical Research*, *92*(A5), 4467–4489. https://doi.org/10.1029/JA092iA05p04467
Holt, J. M., Wand, R. H., Evans, J. V., & Oliver, W. L. (1987). Empirical models for the plasma convection at high latitudes from Millstone Hill observations. *Journal of Geophysical Research*, *92*(A1), 203–212. https://doi.org/10.1029/JA092iA01p00203
Imber, S. M., Milan, S. E., & Lester, M. (2013). The Heppner-Maynard Boundary measured by SuperDARN as a proxy for the latitude of the auroral oval. *Journal of Geophysical Research: Space Physics*, *118*, 685–697. https://doi.org/10.1029/2012JA018222
King, J. H., & Papitashvili, N. E. (2005). Solar wind spatial scales in and comparisons of hourly Wind and ACE plasma and magnetic field data. *Journal of Geophysical Research*, *110*, A02104. https://doi.org/10.1029/2004JA010649
Kivelson, M. G. (1976). Magnetospheric electric fields and their variation with geomagnetic activity. *Reviews of Geophysics*, *14*(2), 189–197. https://doi.org/10.1029/RG014i002p00189
Koustov, A. V., Sofko, G. J., André, D., Dawnskin, D. W., & Benkevitch, L. V. (2004). Seasonal variation of HF radar F region echo occurrence in the midnight sector. *Journal of Geophysical Research*, *109*, A06305. https://doi.org/10.1029/2003JA010337
Koustov, A. V., Yakymenko, K. N., & Ponomarenko, P. V. (2017). Seasonal effect for polar cap sunward plasma flows at strongly northward IMF B_z. *Journal of Geophysical Research: Space Physics*, *122*, 2530–2541. https://doi.org/10.1029/2016JA023556
Kunduri, B. S. R., Baker, J. B. H., Ruohoniemi, J. M., Thomas, E. G., Shepherd, S. G., & Sterne, K. T. (2017). Statistical characterization of the large-scale structure of the subauroral polarization stream. *Journal of Geophysical Research: Space Physics*, *122*, 6035–6048. https://doi.org/10.1002/2017JA024131
Lockwood, M., Cowley, S. W. H., & Freeman, M. P. (1990). The excitation of plasma convection in the high-latitude ionosphere. *Journal of Geophysical Research*, *95*(A6), 7961–7972. https://doi.org/10.1029/JA095iA06p07961
Oliver, W. L., Holt, J. M., Wand, R. H., & Evans, J. V. (1983). Millstone Hill incoherent scatter observations of auroral convection over $60^\circ < \Lambda < 75^\circ$: 3. Average patterns versus Kp. *Journal of Geophysical Research*, *88*(A7), 5505–5516. https://doi.org/10.1029/JA088iA07p05505
Oksavik, K., Greenwald, R. A., Ruohoniemi, J. M., Hairston, M. R., Paxton, L. J., Baker, J. B. H., et al. (2006). First observations of the temporal/spatial variation of the sub-auroral polarization stream from the SuperDARN Wallops HF radar. *Geophysical Research Letters*, *33*, L12104. https://doi.org/10.1029/2006GL026256
Papitashvili, V. O., & Rich, F. J. (2002). High-latitude ionospheric convection models derived from Defense Meteorological Satellite Program ion drift observations and parameterized by the interplanetary magnetic field strength and direction. *Journal of Geophysical Research*, *107*(A8), 1198. https://doi.org/10.1029/2001JA000264
Papitashvili, V. O., Belov, B. A., Faermark, D. S., Feldstein, Y. I., Golyshev, S. A., Gromova, L. I., & Levitin, A. E. (1994). Electric potential patterns in the northern and southern polar regions parameterized by the interplanetary magnetic field. *Journal of Geophysical Research*, *99*(A7), 13,251–13,262. https://doi.org/10.1029/94JA00822
Papitashvili, V. O., Rich, F. J., Heinemann, M. A., & Hairston, M. R. (1999). Parameterization ofthe Defense Meteorological Satellite Program ionospheric electrostatic potentials by the interplanetary magnetic field strength and direction. *Journal of Geophysical Research*, *104*(A1), 177–184. https://doi.org/10.1029/1998JA900053
Pettigrew, E. D., Shepherd, S. G., & Ruohoniemi, J. M. (2010). Climatological patterns of high-latitude convection in the Northern and Southern hemispheres: Dipole tilt dependencies and interhemispheric comparisons. *Journal of Geophysical Research*, *115*, A07305. https://doi.org/10.1029/2009JA014956
Peymirat, C., & Fontaine, D. (1997). Polar cap convection patterns inferred from EISCAT observations. *Annales de Geophysique*, *15*, 403–411. https://doi.org/10.1007/s00585-997-0403-9
Ponomarenko, P., Nishitani, N., Oinats, A. V., Tsuay, T., & St.-Maurice, J.-P. (2016). Application of ground scatter returns for calibration of HF interferometry data. *Earth, Planets and Space*, *67*, 138. https://doi.org/10.1186/s40623-015-0310-3
Qian, L., Burns, A. G., Emery, B. A., Foster, B., Lu, G., Maute, A., et al. (2014). The NCAR TIE-GCM. In J. Huba, R. Schunk, & G. Khazanov (Eds.), *Modeling the Ionosphere-Thermosphere System*. Chichester, UK: John Wiley. https://doi.org/10.1002/9781118704417.ch7
Reiff, P. H., & Burch, J. L. (1985). IMF By-dependent plasma flow and Birkeland currents in the dayside magnetosphere: 2. A global model for northward and southward IMF. *Journal of Geophysical Research*, *90*(A2), 1595–1609. https://doi.org/10.1029/JA090iA02p01595

Rich, F. J., & Hairston, M. R. (1994). Large-scale convection patterns observed by DMSP. *Journal of Geophysical Research*, *99*(A3), 3827–3844. https://doi.org/10.1029/93JA03296

Ridley, A. J., Crowley, G., & Freitas, C. (2000). An empirical model of the ionospheric electric potential. *Geophysical Research Letters*, *27*(22), 3675–3678. https://doi.org/10.1029/1999GL011161

Ridley, A. J., Deng, Y., & Tóth, G. (2006). The global ionosphere–thermosphere model. *Journal of Atmospheric and Solar-Terrestrial Physics*, *68*, 839–864. https://doi.org/10.1016/j.jastp.2006.01.008

Ruohoniemi, J. M., & Baker, K. B. (1998). Large-scale imaging of high-latitude convection with Super Dual Auroral Radar Network HF radar observations. *Journal of Geophysical Research*, *103*(A9), 20,797–20,811. https://doi.org/10.1029/98JA01288

Ruohoniemi, J. M., & Greenwald, R. A. (1995). Observations of IMF and seasonal effects in high-latitude convection. *Geophysical Research Letters*, *22*(9), 1121–1124. https://doi.org/10.1029/95GL01066

Ruohoniemi, J. M., & Greenwald, R. A. (1996). Statistical patterns of high-latitude convection obtained from Goose Bay HF radar observations. *Journal of Geophysical Research*, *101*(A10), 21,743–21,763. https://doi.org/10.1029/96JA01584

Ruohoniemi, J. M., & Greenwald, R. A. (1997). Rates of scattering occurrence in routine HF radar observations during solar cycle maximum. *Radio Science*, *32*(3), 1051–1070. https://doi.org/10.1029/97RS00116

Ruohoniemi, J. M., & Greenwald, R. A. (2005). Dependencies of high-latitude plasma convection: Consideration of interplanetary magnetic field, seasonal, and universal time factors in statistical patterns. *Journal of Geophysical Research*, *110*, A09204. https://doi.org/10.1029/2004JA010815

Ruohoniemi, J. M., Barnes, R. J., Greenwald, R. A., & Shepherd, S. G. (2001). The response of the high-latitude ionosphere to the coronal mass ejection event of April 6, 2000: A practical demonstration of space weather nowcasting with the Super Dual Auroral Radar Network HF radars. *Journal of Geophysical Research*, *106*(A12), 30,085–30,097. https://doi.org/10.1029/2000JA000217

Senior, C., Fontaine, D., Caudal, G., Alcaydé, D., & Fontanari, J. (1990). Convection electric fields and electrostatic potential over $61^\circ < \Lambda < 72^\circ$ invariant latitude observed with the European incoherent scatter facility. 2. Statistical results. *Annales de Geophysique*, *8*(4), 257–272. https://doi.org/10.5194/angeo-26-823-2008

Shepherd, S. G. (2014). Altitude-adjusted corrected geomagnetic coordinates: Definition and functional approximations. *Journal of Geophysical Research: Space Physics*, *119*, 7501–7521. https://doi.org/10.1002/2014JA020264

Shepherd, S. G. (2017). Elevation angle determination for SuperDARN HF radar layouts. *Radio Science*, *52*, 938–950. https://doi.org/10.1002/2017RS006348

Shepherd, S. G., & Ruohoniemi, J. M. (2000). Electrostatic potential patterns in the high-latitude ionosphere constrained by SuperDARN measurements. *Journal of Geophysical Research*, *105*(A10), 23,005–23,014. https://doi.org/10.1029/2000JA000171

Shue, J.-H., Chao, J. K., Fu, H. C., Russell, C. T., Song, P., Khurana, K. K., & Singer, H. J. (1997). A new functional form to study the solar wind control of the magnetopause size and shape. *Journal of Geophysical Research*, *102*(A5), 9497–9511. https://doi.org/10.1029/97JA00196

Sojka, J. J., Rasmussen, C. E., & Schunk, R. W. (1986). An interplanetary magnetic field dependent model of the ionospheric convection electric field. *Journal of Geophysical Research*, *91*(A10), 11,281–11,290. https://doi.org/10.1029/JA091iA10p11281

Thomas, E. G., Baker, J. B. H., Ruohoniemi, J. M., Clausen, L. B. N., Coster, A. J., Foster, J. C., & Erickson, P. J. (2013). Direct observations of the role of convection electric field in the formation of polar tongue of ionization from storm enhanced density. *Journal of Geophysical Research: Space Physics*, *118*, 1180–1189. https://doi.org/10.1002/jgra.50116

SuperDARN Data Analysis Working Group. Participating members, Thomas, E. G., Ponomarenko, P. V., Bland, E. C., Burrell, A. G., Kotyk, K., et al. (2017). SuperDARN Radar Software Toolkit (RST) 4.0 (Version v4.0). Zenodo. https://doi.org/10.5281/zenodo.801459

SuperDARN Data Analysis Working Group. Participating members, Thomas, E. G., Ponomarenko, P. V., Bland, E. C., Burrell, A. G., Kotyk, K., et al. (2018). SuperDARN Radar Software Toolkit (RST) 4.1 (Version v4.1). Zenodo. https://doi.org/10.5281/zenodo.1143675

Thébault, E., Finlay, C. C., Beggan, C. D., Alken, P., Aubert, J., Barrois, O., et al. (2015). International Geomagnetic Reference Field: The 12th generation. *Earth, Planets and Space*, *67*, 79. https://doi.org/10.1186/s40623-015-0228-9

Thomsen, M. F. (2004). Why Kp is such a good measure of magnetospheric convection. *Space Weather*, *2*, S11004. https://doi.org/10.1029/2004SW000089

Yakymenko, K. N., Koustov, A. V., & Fiori, R. A. D. (2018). Interhemispheric asymmetry of the sunward plasma flows for strongly dominant IMF $B_Z > 0$. *Journal of Geophysical Research: Space Physics*, *123*, 315–325. https://doi.org/10.1002/2017JA024644

Weimer, D. R. (1995). Models of high-latitude electric potentials derived with a least error fit of spherical harmonic coefficients. *Journal of Geophysical Research*, *100*(A10), 19,595–19,607. https://doi.org/10.1029/95JA01755

Weimer, D. R. (1996). A flexible, IMF dependent model of high-latitude electric potentials having “space weather” applications. *Geophysical Research Letters*, *23*(18), 2549–2552. https://doi.org/10.1029/96GL02255

Weimer, D. R. (2001). An improved model of ionospheric electric potentials including substorm perturbations and application to the Geospace Environment Modeling November 24, 1996 event. *Journal of Geophysical Research*, *106*(A1), 407–416. https://doi.org/10.1029/2000JA000604

Weimer, D. R. (2005). Improved ionospheric electrodynamic models and application to calculating Joule heating rates. *Journal of Geophysical Research*, *110*, A05306. https://doi.org/10.1029/2004JA010884

Zhang, S.-R., Holt, J. M., & McCready, M. (2007). High latitude convection based on long-term incoherent scatter radar observations in North America. *Journal of Atmospheric and Solar-Terrestrial Physics*, *69*, 1273–1291. https://doi.org/10.1016/j.jastp.2006.08.017

Zou, S., Lyons, L. R., Wang, C.-P., Boudouridis, A., Ruohoniemi, J. M., Anderson, P. C., et al. (2009). On the coupling between the Harang reversal evolution and substorm dynamics: A synthesis of SuperDARN, DMSP, and IMAGE observations. *Journal of Geophysical Research*, *114*, A01205. https://doi.org/10.1029/2008JA013449

Erratum

A correction has been made to section 2 to better acknowledge the SuperDARN Data Analysis Working Group. Tables 1 and 2 have also been reformatted to make them easier to read, and the present version may be considered the authoritative version of record.